A COMPUTATIONAL APPROACH TO OPTICAL AND CHARGE CARRIER PROPERTIES OF ORGANIC SEMICONDUCTORS

by
Haydar Taylan TURAN
B.S., Chemistry, Ege University, 2014

Submitted to the Institute for Graduate Studies in
Science and Engineering in partial fulfillment of
the requirements for the degree of
Master of Science

Graduate Program in Chemistry
Boğaziçi University
2016

A COMPUTATIONAL APPROACH TO OPTICAL AND CHARGE CARRIER PROPERTIES OF ORGANIC SEMICONDUCTORS

APPROVED BY:

Prof. Viktorya Aviyente ……………………...
(Thesis Supervisor)

Assoc. Prof. Nursel Acar Selçuki ……………………...

Assoc. Prof. Şaron Çatak ……………………..

DATE OF APPROVAL: 23.12.2016

To My Family

ACKNOWLEDGEMENTS

I would like to express my sincere gratitude to my thesis advisor Prof. Dr. Viktorya Aviyente for her support, patience and guidance.

I wish to extend my appreciation to the members of my committee: my bachelor degree advisor Assoc. Prof. Nursel Acar Selçuki (Ege University) and Assoc. Prof. Şaron Çatak for their valuable advices and comments.

I gratefully acknowledge Prof. Antonio Monari (University of Lorraine) for his advices, comments and his scientific guidance during my stays in University of Lorraine Also, I acknowledge Dr. Marco Marazzi and Dr. Mariachiara Pastore for their advices and scientific guidance.

My hearty thanks go to all current and former members of Computational Chemistry and Biochemistry group (CCBG) for their friendship and support.

Finally, I would like to express deepest gratitude to my mother and father for their continuous love and support throughout my life.

ABSTRACT

In this study, the structural and optical properties of various organic semiconductors have been computationally investigated.

In the first part, linear and nonlinear optical properties of a series of bis(E-dimesitylborylethenyl)-substituted arenes have been modeled by high-level computational protocols. The former compounds show a remarkable interest as infrared two-photon absorbers and hence may be used in the field of optical active and smart materials or for energy storage purposes. Excited state topologies, absorption and emission spectra, excited state metrics, natural transition orbitals and two-photon absorption cross-section of a series of chromophores have been computed by means of density functional theory (DFT) and time dependent DFT (TD-DFT). Extended benchmark tests on the performance of different functionals have been used. Dynamic and vibronic effects on absorption and emission spectra have been taken into account by sampling the conformational space by means of the Wigner distribution. Important infrared two photon absorption cross sections involving transitions to the second excited state have been observed.

In the second part, aim of the study was to understand the unusual electron mobility loss of a bifuran derivative. A benchmark test was performed to choose the ideal functional/basis set combination. Potential energy scans, reorganization energies and transfer integrals of two bifuran and bithiophene derivatives have been performed to analyze intramolecular and intermolecular charge transfers in the molecules. The study shows that lack of intermolecular charge transportation was the reason behind the electron mobility loss in the bifuran derivative compared to the bithiophene derivative.

ÖZET

Bu çalışmada, çeşitli organik yarı iletkenlerin optik ve yapısal özellikleri hesapsal olarak incelendi.

Birinci kısımda, bis(E-dimesitylborylethenyl)-sübsitiye arenlerin lineer ve lineer olmayan optik özellikleri yüksek seviye hesapsal protokollar kullanarak modellendi. Bahsi geçen moleküller, dikkat çekici kızıl ötesi iki foton absorbsiyon özellikleri nedeniyle, optikçe aktif, akıllı materyal olarak enerji depolama amacıyla kullanabileceklerini gösterdiler. Kromoforların, uyarılmış hal topolojileri, absorpsiyon ve emisyon spektrumları, uyarılmış hal indeksleri, doğal geçiş orbitalleri ve iki-foton absorpsiyon özellikleri, Yoğunluk Fonksiyonel Teorisi (DFT) ve Zamana Bağlı Yoğunluk Fonksiyonel Teorisi (TD-DFT) ile incelenmiştir. Farklı fonksiyonelleri kapsayan geniş bir karşılaştırma testi yapılmıştır. Dinamik ve titreşim etkilerinin absorpsiyon ve emisyon üstüne etkileri, Wigner dağılımı kullanılarak konformasyonel alan örnekleri yardımıyla gerçekleştirilmiştir. İkinci uyarılmış hale geçiş sırasında, dikkate değer iki-foton absorpsiyon değerleri gözlenmiştir.

İkinci kısımda, çalışmanın amacı bifuran türevinde gözlemlenen olağan dışı elektron mobilite kaybının nedenini bulmaktır. İdeal fonksiyonel/baz set kombinasyonunu bulmak için mukayeseli bir çalışma yapılmıştır. Bifuran ve bitiyofen türevlerinin potensiyel enerji taramaları, reorganizasyon enerjileri ve transfer integralleri molekül içi ve moleküller arası yük transferlerini saptamak için incelenmiştir. Çalışma, elekton mobilite kaybının arkasındaki nedenin moleküller arası yük taşımadan kaynaklanabildiğini göstermiştir.

TABLE OF CONTENTS

ACKNOWLEDGEMENTS...iv

ABSTRACT..v

ÖZET vi

LIST OF FIGURES……………………………………………………………...ix

LIST OF TABLES……………………………………………………………....xi

LIST OF SYMBOLS/ABBREVIATIONS………………………………………..xii

1.INTRODUCTION 1

2. METHODOLOGY 7

2.1. Density Functional Theory...7

2.2. Time Dependent Density Functional Theory...12

2.3. Basis Sets 14

2.4. Continuum Solvation Models 15

3. AIM OF THE STUDY 17

4. ASSESING ONE- AND TWO- PHOTON OPTICAL PROPERTIES OF BORON CONTANING ARENES 18

4.1 Introduction..18

4.2 Methodology 21

4.2.1 Wigner Distribution Function...21

4.2.2. ϕ_S Index 22

4.2.3 Computational Procedure 24

4.3. Results and Discussion...27

4.3.1 Excited States Topology and NTO...30

4.3.2 Dynamic Effects on Optical Properties 38

4.3.3 Two-photon absorption 42

4.4 Conclusion..44

5. UNDERSTANDING THE IMPACT OF THIOPHENE/FURAN SUBSTITUTION TO INTRINSIC CHARGE-CARRIER MOBILITY..47

5. 1. Introduction..47

5.2. Methodology..49

5.2.1 Reorganization Energies..49

5.2.2. Transfer Integrals..51

5.3.Results…………………………………………………………………………...53

5.3.1. Geometrical Parameters……………………………………………….....53

5.3.2. Reorganization Energies..58

5.3.3. Charge Transfer Integrals of the Crystals...60

5.4. Conclusion and Future Work..62

REFERENCES..63

LIST OF FIGURES

Figure 1.1 Device Structure for a) Single layer b) Bilayer c) Bulk Heterojunction Organic Photovoltaic cells 3

Figure 1.2 Fundamental steps of charge transfer occurring in donor-acceptor heterojunction solar cells 5

Figure 4.1 Chemical formulae of the (E-dimesitylborylethenyl)-substituted arenes investigated in this thesis 18

Figure 4.2 Graphical depiction of the Φ_S descriptor as the overlap between detachment and attachment densities 24

Figure 4.3 Results of the Wigner distribution calculations for absorption spectra of each family. All the vertical transitions have been convoluted with Gaussian functions of fixed width at half-length of 0.2 eV 41

Figure 4.4 Results of the Wigner distribution calculations for emission spectra of each family. All the vertical transitions have been convoluted with Gaussian functions of fixed width at half-length of 0.3 eV 42

Figure 5.1 Structures of the bi-T (top) and bi-F (bottom) 48

Figure 5.2 Internal reorganization energy $\lambda_{+} + \lambda_{-}$ for hole transfer, and the adiabatic ionization energy 49

Figure 5.3 Internal reorganization energy $\lambda_{+} + \lambda_{-}$ for electron transfer, and the adiabatic ionization energy 50

Figure 5.4 PES of bi-F 58

Figure 5.5 PES of bi-T 58

Figure 5.6 Solid state packing of the molecules 61

LIST OF TABLES

Table 4.1. Benchmark calculations for absorption. λ_{Max} values are given in nm and values in parenthesis represent the excitation energies given in eV 27

Table 4.2 Benchmark calculations and experimental results for absorption including solvent effects. λ_{Max} values are given in nm, and values in parenthesis represent the excitation energies given in eV 29

Table 4.3 Benchmark calculations and experimental results for emission. λ_{Max} values are given in nm, and in parenthesis, in eV...................................... 30

Table 4.4 Virtual and Occupied NTO’s of A1……………………………….……….30

Table 4.5 Virtual and Occupied NTO’s of A2……………………………….……….31

Table 4.6 Virtual and Occupied NTO’s of A3……………………………….……….32

Table 4.7 Virtual and Occupied NTO’s of B1……………………………….……….33

Table 4.8 Virtual and Occupied NTO’s of B2……………………………….……….34

Table 4.9 Virtual and Occupied NTO’s of B3……………………………….……….34

Table 4.10 Virtual and Occupied NTO’s of C1……………………………….……….35

Table 4.11 Calculated (ωB97XD/6-31G*//B3LYP/6-31G*) Φs for absorption (Φ_{Ab}) and emission (Φ_{Em}) values of the singlets.. 37

Table 4.12 Calculated Wigner Distribution Results in toluene and DCM for absorption (ωB97XD/6-31G*//B3LYP/6-31G*).. 38

Table 4.13 Experimental and calculated (ωB97XD/6-31G*//B3LYP/6-31G*) λ_{Max} in DCM, via Wigner procedure. Corresponding absorption and emission maxima are given in nm and, in parenthesis, in eV...................... 40

Table 4.14 Calculated two photon absorption cross-sections and absorption wavelengths 44

Table 5.1 Calculated and experimental hole reorganization energies (meV) of rubrene and pentacene 54

Table 5.2 Selected bond lengths (Å), dihedral angles (Φ in °) of bi-F and bi-T at B3LYP/6-311G** level in $CHCl_3$ (Φ_1 = C1-C2-C3-X1, Φ_2= X1-C5-C6-X2, Φ_3= X2-C8-C9-C10) Experimental values are given in parenthesis 54

Table 5.3 BLA of Bi-F (Å)…………………………………………………………...56

Table 5.4 BLA of Bi-T (Å)…………………………………………………………...56

Table 5.5 Bond length (Å) and dihedral angle (Φ in °) changes of bi-F and bi-T upon oxidation and reduction at B3LYP/6-311G** level in $CHCl_3$ (Φ_1 = C1-C2-C3-C4, Φ_2= X1-C5-C6-X2, Φ_3= C7-C8-C9-C10) 56

Table 5.6 Calculated (B3LYP/6-311G**) Reorganization Energies (meV), VIP, AIP, VEA and AEA (eV) in $CHCl_3$. Experimental values are given in parenthesis 59

Table 5.7 Calculated Transfer Integrals (meV), centroid to centroid distances (Å) of Bi-F and Bi-T 61

LIST OF SYMBOLS

$E^{\ddagger}$	Electronic activation energy
E_c^{VWN}	Vosko-Wilk-Nusair correlation functional
E_x^{exact}	Exact exchange energy
$E_c[\rho]$	Correlation energy
$E_x[\rho]$	Exchange energy
$E_{\sigma\sigma*}$	Non-covalent contributions to the energy
$G^{\ddagger}$	Gibbs free energy of activation
$J[\rho]$	Coulomb energy
$T[\rho]$	Kinetic energy of interacting electrons
$T_s[\rho]$	Kinetic energy of non-interacting electrons
U_x^{σ}	Exchange energy density
$V_{\mathrm{ee}}[\rho(\mathbf{r})]$	Interelectronic interactions
$V_{\mathrm{ext}}(\mathbf{r})$	External potential
V_{KS}	Kohn-Sham potential

ΔE_x^{B88}	Becke’s gradient correction
ΔE_0	Relative electronic energy at 0 K
ΔE_{0+ZPE}	Sum of the change in electronic energy and zero point energy at 0 K
ΔH_{rxn}	Heat of reaction as electronic energy
$v(r)$	External potential
$\rho(r)$	Electron density
ψi	Kohn-Sham orbitals
ϕ_s	Quantitative Topological Descriptor
Γ	Detechment density matrix
Λ	Attachment density matrix
λ_{ij}	Reorganization Energy
Ψ	Many electron wavefunction

LIST OF ACRONYMS/ABBREVIATIONS

ADF	Amsterdam Density Functional
B3LYP	Becke-3-parameter Lee-Yang-Parr functional
B88	Becke 88 Exchange Functional
BLA	Bond Length Alternation
BMK	Boese-Martin for Kinetics
DFT	Density functional theory
TD-DFT	Time Dependent Density Functional Theory
GGA	Generalized Gradient Approximation
$\hat{H}$	Hamiltonian operator
h_i	One-electron hamiltonian
HOMO	Highest Occupied Molecular Orbital
HF	Hartree-Fock
J_{ij}	Charge transfer integral
K	Exchange Integral
KS	Kohn-Sham
k_{ij}	Electron Transfer Rate
LC	Long-range Corrected
LDA	Local Density Approximation
LUMO	Lowest Unoccupied Molecular Orbital
M06-2X	Empirical exchange-correlation functional
M06-HF	Empirical exchange-correlation functional with %100 HF
MPWB1K	Modified Perdew-Wang-Becke 1 Parameter Method for Kinetic

1. INTRODUCTION

Carbon based fossil fuels are still the primary energy source for the World's energy needs. Despite the increasing energy demand globally, fossil fuels are expected to be consumed away in the near future. Furthermore, their serious negative effects to the environment are the major issues for fossil fuels; especially, the greenhouse effect caused by severe atmospheric pollution through carbon dioxide emission is a major treat for global warming. Also, carbon dioxide emission has serious negative effects on ocean ecosystem as well as land ecosystem [1].

Finding solutions to prevent the environmental damages and ensure environmental sustainability have been the subject of extensive research in recent years. Environmental sustainability refers to systematic conditions that human activities do not disturb natural cycles more than planetary resilience allows; while do not impoverish the natural capitals that have to be saved for the future generations. Alternative and renewable energy sources such as wind, hydraulic, geothermal and solar energy are the perfect sources to provide formerly mentioned phenomena to our lives.

Solar energy has the highest theoretical energy potential, compared to other alternative energy sources, that is about 89000 terawatts (TW) [2] 13 TW energy is needed in order to sustain lifestyle of 6.5 billion people and research are shown humanity will need an extra 10 TW energy to maintain the current life style [3]. Furthermore, solar energy has advantages of environmental cost, abundance and sustainability compared to the formerly mentioned alternative energy sources. Hereby, increasing the efficiency of harvesting sunlight is crucial to compensate the energy demand in a carbon-free way.

Increasing the efficiency of harvesting sunlight, converting it to electrical energy and store it in a cost-efficient way is a still challenge to overcome. However, economical problem is not the only issue for solar energy systems. Improvement of harvest-convert-store cycle in a convenient commercial form still depends on advancements in science and engineering. The main target is to achieve that is to fabricate more efficient materials while decreasing the production costs. Current commercialized solar cells are based on inorganic materials such as Si, CdTe and $CuIn_{1-x}Ga_xSe_2$ [4, 5]. Also, organic solar cells, dye sensitized solar cells and perovskite solar cells are available in the market. However, despite the advancement in the area of dye sensitized and perovskite solar cells, inorganic solar cells have 85% of the market cell via single of multi crystalline p-n silicon solar cells. [6] Silicon based solar cells have, n-type and p-type, p-type and n-type, alternant crystal stacking to produce direct electric current via enabling the charge deposition and capture between the layers and upon photovoltaic effect. The obtained current maybe stored in a battery or used immediately. The disadvantages of these solar cells are fabrication problems, high purity needs, energy needs during fabrication and production costs.

CdTe based solar cells are another class in inorganic solar cell family. CdTe, has high absorption coefficient, convenient band with a high decomposition temperature, thermal and chemical stability. However, health and safety issues of Cd and high price of the Te are the major disadvantages of this type of solar cells.

Dye sensitized solar cells [7] (DSSC) have, dye molecules to make absorption of sunlight possible. A mesoporous layer composed particles of wide band gap semiconductor oxide such as TiO_2, dye and electrolyte (iodide/triiodide) are present within the cell. Upon photo-excitation dye injects an electron to the conduction band of TiO_2 and is generated by hole injection in a redox electrolyte. After the diffusion of the charges to anode and cathode contacts, electrical current can be obtained. The difference of the Fermi level and conductors corresponds to the open circuit voltage.

Another type of solar cells is the perovskite solar cells [8]. Perovskite structure refers to class of compounds which have the same type of crystal structure as $CaTiO_3$ (calcium titanium oxide). Perovskite solar cells have the advantages of hybrid structure of organic and inorganic materials. Organic parts of the cell has a good solubility and facilitate self-assembly, also effectively enabling its precipitation/deposition from solution; inorganic part of the cell produces an extended network by covalent and/or ionic interactions. Strong interactions allow the precise crystalline structure in deposited films. Despite the high efficiency, perovskite solar cells still suffer from major degradation problems.

Even though power conversion efficiencies of inorganic photovoltaic cells are relatively high, the toxicity and the low cost-efficiency is unfavorable. Thus, focus on developing organic photovoltaic cells increased dramatically after the millennia. Organic solar cells have advantage over formerly mentioned solar cells in terms of, ease of fabrication, low cost, flexibility, inkjet printability, lightweight and diversity through device structure and materials [9]. Also, a wide variety of material and electrode combinations for new potential devices made it possible to improve cell performance in organic photovoltaic technology as opposed to inorganic solar cells [10].

Several types of device architectures have been developed for organic solar cells. The first developed device type was single layer which contains only an organic electronic material between two electrodes. After that, bilayer structures have been introduced; in this type of organic solar cells, electron donor and electron acceptor materials have been used separately. However, the efficiencies of both of these type of cells were low [9, 10]. Bulk-heterojunction structures are fabricated to overcome the efficiency problems. Dispersed heterojunction helped to increase the interface between electron donor and electron acceptor, thus electron and hole mobility. Devices structures are shown in Figure 1.1.

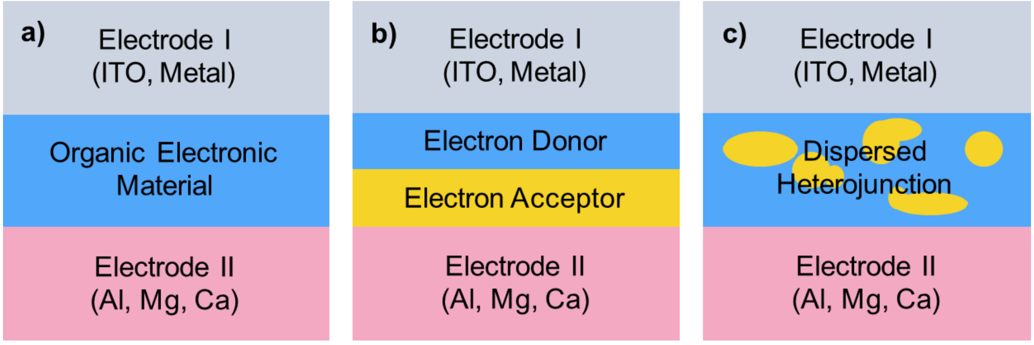

Figure 1.1. Device structure for a) Single layer b) Bilayer c) Bulk Heterojunction Organic Photovoltaic Cells

Low band gap to harvest more sunlight, suitable energy levels to achieve high open circuit voltage (V_{oc}), suitable exciton separation driven force and relatively high molecular weight to promote crystallinity and good hole and electron mobilities are necessities for the materials that are used in organic solar cells [13].

Organic materials that can transport charge carriers are called “Organic Semiconductors”. A typical organic solar cell contains an active layer that has n-type semiconductor as the donor and p-type semiconductor as the acceptor. Indium thin oxide (ITO) is a widely used anode electron that been used in solar cells. Al, Mg and Ca metals are usually chosen as cathode electrode. N-type semiconductor refers to materials that have more electrons than holes and p-type semiconductor refers to materials that have more holes than electrons. Charge carriers are electrons and holes in p orbitals of the semiconductor, and the charge transfer subject of the movement of these carriers from one molecule to the other. Charge movement rate and efficiency is affected by the energy gap between highest occupied molecular orbital (HOMO) of donor and lowest unoccupied molecular orbital (LUMO) of the acceptor. The physical properties of the semiconductor such as HOMO/LUMO levels, hole and electron mobilities, solid state packing can be adjusted by chemical modifications [14].

The mechanism of the charge transport phenomena in p-n junction cells is well understood and described [15]. However, it is not the case for organic semiconductors. Charge transfer mechanism in donor-acceptor bulk heterojunction solar cells illustrated in Figure 1.2.

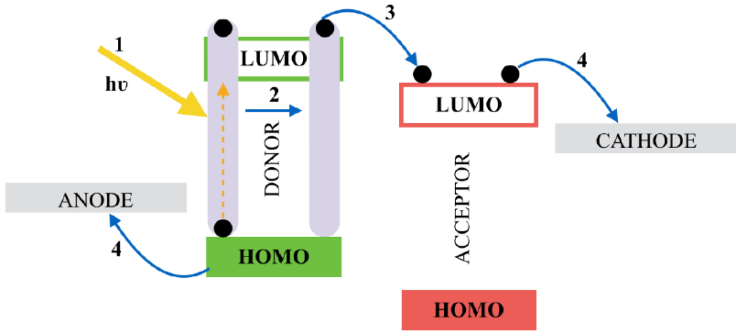

Figure 1.2. Fundamental steps of charge transfer occurring in donor-acceptor heterojunction solar cells

The initial step of the charge transfer mechanism is the formation of an exciton in the donor material. (Step 1) Excitons are formed, instead of electrons in bulk heterojunction solar cells. These excitons have binding energies in between 0.1 eV to 0.5 eV, and they are bound neutral excitonic states. Due to large binding energies free electron and holes cannot be formed from the materials; consequently, direct current cannot be obtained. The excitons need to dissociate first, to diffuse into the donor-acceptor interface (Step 2). The charge recombination occurs if excitons cannot react at the interface. After the diffusion of exciton, dissociation occurs to transport an electron into the acceptor layer (Step 3). As a final step, charge collection occurs at the external electrodes (Step 4)

Power Conversion Efficiency (PCE) is defined as the ratio between the electricity output of the device and the energy of the incoming light. The open circuit voltage V_{OC}, the short circuit current density J_{SC} and the fill factor FF are the parameters that affect the PCE. Short circuit current is related to electron and hole density, and their mobility; increasing the two aforementioned parameters will result in increase in J_{SC}. Also, increasing the thermodynamic driving force of charge separation (ΔG_{CS}) at the donor-acceptor interface, will lead to decrease in electronic excitation energy of the donor. Consequently, the latter can be used to maximize the short circuit current density. V_{OC} is directly related to HOMO level of the donor and LUMO level of the acceptor [14, 15]. V_{OC} can be maximized by decreasing the HOMO energy of the donor and increasing the LUMO energy of the acceptor. However, one should note that, increasing the band gap between HOMO of the donor and LUMO of the acceptor will cause a decrease in J_{SC}. Therefore, to get the maximum potential efficiency, V_{OC} and J_{SC} should be balanced cautiously. FF of the device is determined by the charge carriers reaching the electrodes [18]. Charge separation, mobility of the charge carriers and the morphological and topological properties of the device are the important parameters to maximize the FF.

Acceptor materials used in bulk heterojunction solar cells do not vary much. Soluble fullerene derivatives such as [6,6]-phenyl-C_{61}-butyric acid methyl ester (PCBM) are generally used as the acceptor materials in the cells, since C_{60} has limited solubility [19]. Semiconductors that are used in organic solar cells have different sizes. They can be small molecule organic solar cell (SMOSC), oligomers with structures consisting of a short chain of a repeating unit or polymer chain. Oligothiophenes [20], polythiophenes [16], oligoselenophenes [21], triayrl amines, soluble acenes, diketopyrrolopyrrroles (DPP) [22] can be given as examples of various classes of donor materials. Oligomers are more favorable donor materials to use in organic solar cells compared to small molecules and polymers, due to disadvantages such as electron trapping problems of polymer chains and the stability issues of small molecules. Hereby, as consequence of variety of donor materials, it is important to predict the optical properties, charge transfer efficiency, crystal structure and solid state packing in order to understand the fundamental structure-property relationships.

2. METHODOLOGY

2.1. Density Functional Theory

Density Functional Theory (DFT) [23] is a quantum mechanical approach, which allows to calculate the electronic structure of atoms and molecule based upon a theory proposed by Kohn-Hohenberg [24, 25]. Kohn-Hohenberg theorem states the ground state density is sufficient enough to determine the wavefunction.

The first theorem of the theory states that electron density $\rho(\mathbf{r})$ determines the external potential $V_{ext}(\mathbf{r})$ i. e. the potential due to the nuclei and the second theorem introduces the variational principle. As a result, the electron density can be computed variationally and the wavefunction, energy, position of nuclei and other related problems can be calculated [23, 26].

The electron density is defined as:

$$\rho(x) = N \int \cdots \int |\Psi(x_1, x_2, \cdots, x_n)|^2 dx_1 dx_2 \cdots dx_n \tag{2.1}$$

where x represents both spin and spatial coordinates of electrons.

The electronic energy can be expressed as a functional of the electron density:

$$E[\rho] = \int v(r)\rho(r)dr + T[\rho] + V_{ee}[\rho] \tag{2.2}$$

where $T[\rho]$ is the kinetic energy of the interacting electrons and $V_{ee}[\rho]$ is the interelectronic interaction energy. The electronic energy may be rewritten as

$$E[\rho] = \int v(r)\rho(r)dr + T_s[\rho] + J[\rho] + E_{xc}[\rho] \tag{2.3}$$

with $J[\rho]$ being the coulomb energy, $T_s[\rho]$ being the kinetic energy of the non-interacting electrons and $E_{xc}[\rho]$ being the exchange-correlation energy functional. The exchange-correlation functional is expressed as the sum of an exchange functional $E_x[\rho]$ and a correlation functional $E_c[\rho]$, although it contains also a kinetic energy term arising from the kinetic energy difference between the interacting and non-interacting electron systems. The kinetic energy term, being the measure of the freedom, and exchange-correlation energy, describing the change of opposite spin electrons (defining extra freedom to an electron), are the favorable energy contributions. The Coulomb energy term describes the unfavorable electron-electron repulsion energy and therefore disfavors the total electronic energy [27].

In Kohn-Sham density functional theory, a reference system of independent non-interacting electrons in a common, one-body potential V_{KS} yielding the same density as the real fully-interacting system is considered. More specifically, a set of independent reference orbitals ψ_i satisfying the following particle independent Schrödinger equation are imagined.

$$\left[-\frac{1}{2}\nabla^2 + V_{KS}\right]\psi_i = \varepsilon_i \psi_i \tag{2.15}$$

with the one-body potential V_{KS} defined as

$$V_{KS} = v(r) + \frac{\partial J[\rho]}{\partial \rho(r)} + \frac{\partial E_{xc}[\rho]}{\partial \rho(r)} \tag{2.16}$$

$$V_{KS} = v(r) + \frac{\rho(r')}{|r - r'|} dr' + v_{xc}(r) \tag{2.17}$$

where $v_{xc}(r)$ is the exchange-correlation potential. The independent orbitals ψ_i are known as Kohn-Sham orbitals and give the exact density by

$$\rho(r) = \sum_i^N |\psi_i|^2 \tag{2.18}$$

if the exact form of the exchange-correlation functional is known. However, the exact form of this functional is not known and approximate forms are developed starting with the local density approximation (LDA). This approximation gives the energy of a uniform electron gas, i. e. a large number of electrons uniformly spread out in a cube accompanied with a uniform distribution of the positive charge to make the system neutral. The energy expression is

$$E[\rho] = T_s[\rho] + \int \rho(r)v(r)dr + J[\rho] + E_{xc}[\rho] + E_b \tag{2.19}$$

where E_b is the electrostatic energy of the positive background. Since the positive charge density is the negative of the electron density due to uniform distribution of particles, the energy expression is reduced to

$$E[\rho] = T_s[\rho] + E_{xc}[\rho] \tag{2.20}$$

$$E[\rho] = T_s[\rho] + E_x[\rho] + E_c[\rho] \tag{2.21}$$

The kinetic energy functional can be written as

$$T_s[\rho] = C_F \int \rho(r)^{5/3} dr \tag{2.22}$$

where C_F is a constant equal to 2.8712. The exchange functional is given by

$$E_x[\rho] = -C_x \int \rho(r)^{4/3} dr \tag{2.23}$$

with C_x being a constant equal to 0.7386. The correlation energy, $E_c[\rho]$, for a homogeneous electron gas comes from the parametrization of the results of a set of quantum Monte Carlo calculations.

The LDA method underestimates the exchange energy by about 10 per cent and does not have the correct asymptotic behavior. The exact asymptotic behavior of the exchange energy density of any finite many-electron system is given by

$$\lim_{x \to \infty} U_x^{\sigma} = -\frac{1}{r} \tag{2.24}$$

U_x^{σ} being related to $E_x[\rho]$ by

$$E_x[\rho] = \frac{1}{2} \sum_{\sigma} \int \rho_{\sigma} U_x^{\sigma} dr \tag{2.25}$$

A gradient-corrected functional is proposed by Becke

$$E_x = E_x^{LDA} - \beta \sum_{\sigma} \int \rho_{\sigma}^{4/3} \frac{x_{\sigma}^2}{1 + 6\beta x_{\sigma} \sinh^{-1} x_{\sigma}} dr \tag{2.26}$$

where σ denotes the electron spin, $x_{\sigma} = \dfrac{|\nabla \rho_{\sigma}|}{\rho_{\sigma}^{4/3}}$ and β is an empirical constant (β=0.0042). This functional is known as Becke88 (B88) functional [25].

The adiabatic connection formula connects the non-interacting Kohn-Sham reference system (λ=0) to the fully-interacting real system (λ=1) and is given by

$$E_{xc} = \int_0^1 U_{xc}^{\lambda} d\lambda \tag{2.27}$$

where λ is the interelectronic coupling-strength parameter and U_{xc}^{λ} is the potential energy of exchange-correlation at intermediate coupling strength. The adiabatic connection formula can be approximated by

$$E_{xc} = \frac{1}{2} E_x^{exact} + \frac{1}{2} U_{xc}^{LDA} \tag{2.28}$$

since $U_{xc}^{0} = E_x^{exact}$, the exact exchange energy of the Slater determinant of the Kohn-Sham orbitals, and $U_{xc}^{1} = U_{xc}^{LDA}$ [22].

The closed shell Lee-Yang-Parr (LYP) correlation functional [28] is given by

$$E_c = -a\int \frac{1}{1+d\rho^{-1/3}}\left\{\rho + b\rho^{-2/3}\left[C_F\rho^{5/3} - 2t_w + \left(\frac{1}{9}t_w + \frac{1}{18}\nabla^2\rho\right)\right]e^{-c\rho^{-1/3}}\right\}dr \quad (2.29)$$

where

$$t_w = \frac{1}{8}\frac{|\nabla\rho(r)|^2}{\rho(r)} - \frac{1}{8}\nabla^2\rho \quad (2.30)$$

The mixing of LDA, B88, E_x^{exact} and the gradient-corrected correlation functionals to give the hybrid functionals [29] involves three parameters.

$$E_{xc} = E_{xc}^{LDA} + a_0\left(E_x^{exact} - E_x^{LDA}\right) + a_x\Delta E_x^{B88} + a_c\Delta E_c^{non-local} \quad (2.31)$$

where ΔE_x^{B88} is the Becke's gradient correction to the exchange functional. In the B3LYP functional, the gradient-correction ($\Delta E_c^{non-local}$) to the correlation functional is included in LYP. However, LYP contains also a local correlation term which must be subtracted to yield the correction term only.

$$\Delta E_c^{non-local} = E_c^{LYP} - E_c^{VWN} \quad (2.32)$$

where E_c^{VWN} is the Vosko-Wilk-Nusair correlation functional, a parametrized form of the LDA correlation energy based on Monte Carlo calculations. The empirical coefficients are a_0=0.20, a_x=0.72 and a_c=0.81 [30].

2.2. Time Dependent Density Functional Theory

Time Dependent Functional Theory (TD-DFT) is a quantum mechanical tool for the calculation of electronic exited states. The Hamiltonian Operator can be expressed as

$$\hat{H} = \hat{T}(\underline{r}) + \hat{W}(\underline{r}) + \hat{V}_{ext}(\underline{r}, t) \quad (2.33)$$

The first term denotes the kinetic energy of the electrons, the second term describes the coulomb interactions between the electrons, and the third term defines the influence of time-dependent potential on the electrons. The exicted state energy depends on the external potential. Thus, to calculate the excited state properties it is necessary to know to effects of the potential.

The Hohenberg-Kohn Theorem is applied a variational principle involving the action

$$A = \int_{t_0}^{t_1} \langle \Psi(t) | i \frac{\partial}{\partial_t} - \widehat{H} | \Psi(t) \rangle \, dt \tag{2.34}$$

and the wavefunction is determined up to a time-dependent constant

$$\Psi(\boldsymbol{r}_1, \dots, \boldsymbol{r}_N, t) = \Psi[\rho](t) e^{-i\alpha(t)} \tag{2.35}$$

The phase factor adds a constant to the action in Equation 2.33:

$$A[\rho] = \int_{t_0}^{t_1} \langle \widetilde{\Psi}[\rho](t) | i \frac{\partial}{\partial_t} - \widehat{H}(t) | \widetilde{\Psi}[\rho](t) \rangle \, dt + \alpha(t_1) - \alpha(t_0) = A[\rho] + const. \tag{2.36}$$

And A[ρ] can be written as

$$A[\rho] = B[\rho] - \int d\boldsymbol{r} \int_{t_0}^{t_1} (\boldsymbol{r}, t) \rho(\boldsymbol{r}, t) dtv \tag{2.37}$$

where B[ρ] is independent of the external potential. Assume an independent system which has the property described in Equation 2.38:

$$\rho(\boldsymbol{r}, t) = \sum_i f_i |\Psi_i(\boldsymbol{r}, t)|^2 \tag{2.38}$$

Hence to rewrite B[ρ],

$$B[\rho] = \sum_{\mathrm{i}} \mathrm{f_i} \int_{t_0}^{t_1} \langle \Psi_{\mathrm{i}}(\mathrm{t}) | \mathrm{i}\frac{\partial}{\partial_{\mathrm{t}}} - \frac{1}{2}\nabla_{\mathrm{i}}^{2} | \Psi_{\mathrm{i}}(\mathrm{t}) \rangle \, \mathrm{dtv} - \frac{1}{2}\int_{t_0}^{t_1} \mathrm{dt} \iint \mathrm{d}\mathbf{r}_1 \mathrm{d}\mathbf{r}_2 \frac{\rho(\mathbf{r}_1,\mathrm{t})\rho(\mathbf{r}_2,\mathrm{t})}{|\mathbf{r}_1 - \mathbf{r}_2|} - \mathrm{A_{xc}}[\rho] \quad (2.39)$$

Where $A_{xc}[\rho]$ is the exchange and correlation action functional. Applying the variational principle to (2.37) with constraint

$$\rho(\boldsymbol{r}, t) = \sum_i f_i |\Psi_i(\boldsymbol{r}, t)|^2 = \sum_i^N |\Psi_i(\boldsymbol{r}, t)|^2 \quad (2.40)$$

we obtain the time-dependent Kohn-Sham Equation in Equation 2.41:

$$\left[-\frac{1}{2}\nabla^2 + v_{eff}(\boldsymbol{r}, t)\right] \Psi_i(\boldsymbol{r}, t) = i\frac{\partial}{\partial_t}\Psi_i(\boldsymbol{r}, t) \quad (2.41)$$

$$v_{eff}(\boldsymbol{r}, t) = v_H(\boldsymbol{r}, t) + v_{xc}(\boldsymbol{r}, t) + v_{ext}(\boldsymbol{r}, t) \quad (2.42)$$

and the unknown is now the time-dependent exchange potential, and all exchange and correlation effects in TD-DFT are collected in Equation 2.43:

$$v_{xc}(\boldsymbol{r}, t) = \frac{\delta A_{xc}[\rho]}{\delta \rho(\boldsymbol{r}, t)} \quad (2.43)$$

Time dependent density functional theory equations are exact, there is not any approximations made. However, since the exchange correlation functional is not known, approximations should be introduced.

The adiabatic approximation (AA) is shown in Equation 2.44:

$$v_{xc}[\rho](\boldsymbol{r}, t) = \frac{\delta A_{xc}[\rho]}{\delta \rho(\boldsymbol{r}, t)} \approx \frac{\delta E_{xc}[\rho]}{\delta \rho(\boldsymbol{r})} |_{\rho = \rho(\boldsymbol{r}, t)} \quad (2.44)$$

If the electron densities change, the exchange and correlation potential change instantaneously.

2.3. Basis Sets

Basis sets describe the wavefunctions, and are necessary to solve the Schrödinger Equation. Split valence basis sets of Pople *et al.* are the most common basis sets used. 3-21G, 6-21G, 6-31+G and 6-311G* are the examples. The functions are splitted, i.e. the first number denotes the primitives in the core functions, and the numbers after the hyphen represent the number of primitives used in the valence functions. Two numbers mean valence double-ζ basis, and three numbers mean valence triple-ζ basis. One can add polarization functions, and extend the basis set, describe the system better and have more mathematical flexibility in calculations. Diffuse functions can also be added, where it is not possible for the basis set to provide enough flexibility to include an electron so far away from the core. Diffuse functions are denoted by the "+" sign to heavy atoms, second "+" sing denotes diffuse functions to hydrogen atoms . Polarization functions on non-hydrogen atoms are shown by "*", and if two asterisks "**" are present, it means that the polarization functions are also added to the light atoms, hydrogen and helium.

2.4. Continuum Solvation Models

Continuum solvation models are the most efficient way to include condensed-phase effects into quantum mechanical calculations [31]. The advantage of these models is that they decrease the number of the degrees of freedom of the system by describing them in a continuous way, usually by means of a distribution function [32, 33]. In continuum solvation models, the solvent is represented as a polarizable medium characterized by its static dielectric constant ε and the solute is embedded in a cavity surrounded by this dielectric medium. The total solvation free energy is defined as

$$\Delta G_{solvation} = \Delta G_{cavity} + \Delta G_{dispersion} + \Delta G_{electrostatic} + \Delta \mathrm{G}_{repulsion} \tag{2.45}$$

where ΔG_{cavity} is the energetic cost of placing the solute in the medium. Dispersion interactions between solvent and solute are expressed as $\Delta G_{dispersion}$ which add stabilization to solvation free energy. $\Delta G_{electrostatic}$ is the electrostatic component of the solute-solvent interaction energy. $\Delta G_{repulsion}$ is the exchange solute-solvent interactons not included in the cavitation energy.

The central problem of continuum solvent models is the electrostatic problem described by the general Poisson equation:

$$-\vec{\nabla}\left[\varepsilon(\vec{r})\nabla\vec{V}(\vec{r})\right] = 4\pi\rho_M(\vec{r}) \tag{2.46}$$

simplified to

$$-\nabla^2 V(\vec{r}) = 4\pi\rho_M(\vec{r}) \text{ within } C \tag{2.47}$$

$$-\varepsilon\nabla^2 V(\vec{r}) = 0 \text{ outside } C \tag{2.48}$$

where C is the portion of space occupied by cavity, ε is dielectric function, V is the sum of electrostatic potential V_M generated by the charge distribution ρ_M and the reaction potential V_R generated by the polarization of the dielectric medium:

$$V(\vec{r}) = V_M(\vec{r}) + V_R(\vec{r}) \tag{2.49}$$

The Polarizable Continuum Model (PCM) belongs to the class of polarizable continuum solvation models [34]. In PCM, the solute is embedded in a cavity defined by a set of spheres centered on atoms (sometimes only on heavy atoms), having radii defined by the van der Waals radius of the atoms multiplied by a predefined factor (usually 1.2). The cavity surface is then subdivided into small domains (called tesserae), where the polarization charges are placed. There are three different approaches to carry out PCM calculations. The original method is called Dielectric PCM (D-PCM), the second model is the Conductor-like PCM (C-PCM) [35] in which the surrounding medium is modeled as a conductor instead of a dielectric, and the third one is an implementation whereby the PCM equations are recast in an integral equation formalism (IEF-PCM). The IEF-PCM have been used in this study.

3. AIM OF THE STUDY

This study is composed of two different parts which are mainly about organic semiconductor materials and their applications in organic solar cells.

In the first part of the thesis, various (E-dimesitylborylethenyl)-substituted arenes have been selected to study the properties of compounds possessing the organo-boron (-B-C-) bond. The structural and optical properties of the compounds have been investigated. These molecules have been categorized into three different families based on the nature of the central arene bridge. Family A gathers (A1) 2,5- bis(E-dimesitylborylethenyl)thiophene, (A2) 5,5'-bis(E-dimesitylborylethenyl)-2,2'-bithiophene, (A3) 5,5”-bis(E-dimesitylborylethenyl)-2,2':5',2”-terthiophene; the effect of π-conjugation connected to the increase of the number of conjugated thiophene rings will hence be particularly assessed. Family B includes (B1) 1,4-bis(E-dimesitylborylethenyl)benzene, (B2) 4,4'-bis(E-dimesitylborylethenyl)biphenyl, (B3) 1,4-bis(E-dimesitylborylethenyl)tetrafluorobenzene; hence in this case the effect of a strong electron-attractor group will be tackled, too. Family C has a single molecule (C1) 4,4'-bis(E-dimesitylborylethenyl)tolan that has different features compared to the previous ones, in particular the two phenyl rings are linked by an acetylene moiety giving a different conjugated pattern and enhancing the rigidity of the structure.

In the second part of the thesis, intramolecular and intermolecular properties of a bifuran and bithiophene derivatives are investigated to find the reason of the unusual electron mobility loss that occurs in the bifuran derivative.

4. ASSESSING ONE- AND TWO- PHOTON OPTICAL PROPERTIES OF BORON CONTANING ARENES

4.1 Introduction

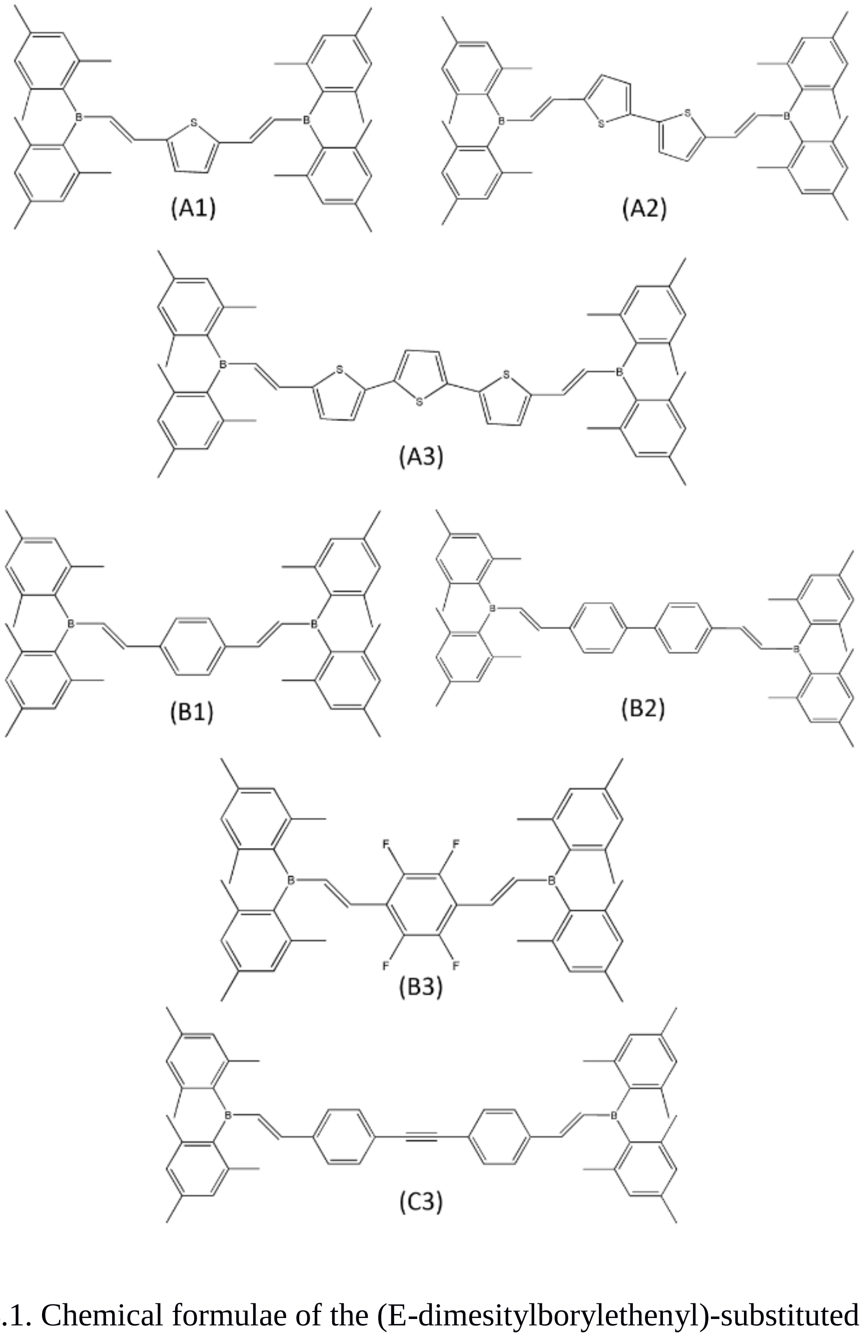

Figure 4.1. Chemical formulae of the (E-dimesitylborylethenyl)-substituted arenes investigated in this paper.

A novel class of compounds, emerging as promising constituents for organic semiconductors is the one of boron derivatives [36, 37]. Indeed, and because of its peculiar electronic structure, three-coordinated boron combines a number of extremely promising features such as: the presence of vacant p-orbitals, the ability of acting as a π-acceptor while remaining σ-donor and a relatively easy complexation with organic molecules [38, [39]. The latter aspect is of particular importance for the possibility it offers to modulate the chemical behavior of the semiconductor by the opportune choice of organic ligands. As an example, bulky substituents can be included in order to provide steric protection improving stability in the presence of oxygen and humidity, i.e. in oxidative conditions. For instance, mesityl groups are used as bulky groups to inhibit the degradation mechanisms [40].

As far as the optical properties are concerned, one of the most sought properties for organic moieties is the extension of the absorption toward the low-energy region of the spectrum (red or near infrared wavelengths). A possibility to achieve such a goal is to switch from one-photon to two-photon absorption (TPA). Indeed, TPA is clearly a hot topic with applications in medicine (localized photodynamic therapy) [41], laser scanning microscopy [42], 3-D optical data storage, micro fabrication and bio-imaging [43]. Physically TPA is produced by the simultaneous absorption of two photons of identical or different frequencies in order to excite a molecule from one state (usually the ground state) to a higher energy electronic state [44]. If we consider photons of equal energy (i.e. a monochromatic laser source), the energy difference between the involved lower and upper electronic states will be equal to twice the energy of a single photon. As such TPA spectra will appear at much longer wavelengths than conventional absorption, and one may access the target excited state with a photon having twice the wavelength corresponding to the exact energy difference. Because of the required simultaneous absorption of two photons TPA is a non-linear optical process; hence its probability depends on the square of the source’s intensity. However this property implies that TPA can eventually dominate over the linear absorption at high intensity [45]. Furthermore the non-linear nature of TPA also allows to increase the selectivity, since because of the need of high intensity, TPA is restricted only to the focal center of the light source (laser); the latter property has of course extremely positive outcomes especially in photodynamic therapy, memory storage and device miniaturization. TPA absorption is dependent on the chromophore hyperpolarizability, as such a positive factor to enhance TPA cross-section includes the presence of extended conjugated moieties and substitution by strong donor or acceptor groups. Conjugated boron containing materials have recently demonstrated their TPA efficiency in several fields [46].

Large-scale quantum mechanical calculations, offering an accurate prediction of the ground and excited state properties of complex materials [47–51], as well as an atomic scale and even electronic resolution of the complex (photo)-chemical pathways responsible for the material functions [52–56], would represent an extremely powerful and low-cost tool in the *in silico* design of new candidate molecules [57–60]. Since many smart materials are able to perform light-induced functions, a good tune and control of their excited state evolution is required. From a molecular modeling point of view this in turn necessitates to tackle electronic excited state properties. In particular the influence of dynamic and vibrational effects on their photo physical or optical properties is crucial, and should be properly taken into account in order to rationalize and predict the relation between structure and functions in organic-based devices. Hence suitable excited state methods, with a good ratio between computational cost and performance, as well as the capacity to model complex photochemical pathways, are required. It is well-known that for organic molecules with spatially extended π systems and push-pull organic systems characterized by charge transfer (CT) excitations, the calculation of the optical absorption spectra is a severe challenge for standard time-dependent density functional theory (TD-DFT) approaches [61–63]. Even if the use of an increased amount of non local Hartree-Fock exchange [64] or range-separated approaches [65–68] practically overcomes the systematic underestimation of the CT excitation energies, the choice of the best DFT functional still remains system dependent. Hence, when dealing with novel organic molecules characterized by large conjugated π frameworks, a systematic benchmark evaluation of different DFT/TD-DFT results against highly correlated wave-function methods or experimental observables are mandatory before defining a reliable computational protocol for predictive purposes.

In order to assess the excited state properties of the different families a rather complete and exhaustive benchmark has been performed including DFT and ab-initio based methodologies. Excitation energies and oscillator strengths have been calculated at TD-DFT level as well as using multireference second order perturbation theory (CAS-PT2). Different functionals have been employed, including double-hybrid approaches [69, 70].

Most importantly the dynamic and vibrational effects have been taken into account using an evolution of a protocol currently used in our laboratory and consisting in exploring the ground (excited) state conformational space by using a Wigner distribution obtained from the vibrational frequencies (Hessians), the final spectrum being obtained by convoluting the vertical excitations obtained from the representative snapshots. The necessity to include molecular vibrational effects, and in particular of out-of-plane low frequency high amplitude displacements, on extended π-conjugated chromophores will be particularly addressed.

4.2 Methodology

4.2.1 Wigner Distribution Function

Wigner distribution function is a quantum correction to classical mechanic, which is used to perform time-frequency analysis [71] Aim of the theory is to link the wavefunction that in appears in Schrödinger's equation to a probability distribution in phase space.

The Wigner distribution *P(x,p)* is defined as:

$$P(x,p)=\frac{1}{\pi\hbar}\int_{-\infty}^{\infty}\psi^{*}(x+y)\psi(x-y)e^{2ipy/\hbar}dy \qquad (2.50)$$

where ψ is wavefunction, x is the position and p is the momentum of any conjugate pair. It is symmetric in x and p.

$$P(x,p)=\frac{1}{\pi\hbar}\int_{-\infty}^{\infty}\varphi^{*}(p+q)\psi(p-q)e^{2ipy/\hbar}dq \qquad (2.51)$$

where φ is the Fouirer transform of ψ

In 3D:

$$P(\overrightarrow{r},\vec{p})=\frac{1}{(2\pi)^{3}}\int\psi^{*}\left(\vec{r}+\frac{\hbar\vec{s}}{2}\right)\psi\left(\vec{r}-\frac{\hbar\vec{s}}{2}\right)e^{i\vec{p}.\vec{s}}d^{3}s \qquad (2.52)$$

when case includes mixed states, it is the Wigner tranform of the density matrix

$$P(x,p) = \frac{1}{\pi\hbar}\int_{-\infty}^{\infty}\langle x+y|\hat{\rho}|x-y\rangle e^{-2ipy/\hbar}dy \tag{2.53}$$

4.2.2. ϕ_S Index

ϕ_S [72] index is a quantitative topological descriptor of photoinduced electronic charge density variation. ϕ_S index is a simple and efficient way to quantitatively evaluate how easy the charge separation is made upon the chromophore's light absorption.

One can obtain the density matrices corresponding to the ground state (P_0), to X^{th} excited state (P_x) and the basis set overlap matrix (S) from excited states quantum-chemical calculations of a N-electron system with a K-sized basis set. Consequently, it is possible to derive Δ matrix as the difference between excited P_x and ground state P_0 density matrix.

$$\Delta = \mathrm{P_X} - \mathrm{P_0} \;\Rightarrow\; \textstyle\sum_{\mathrm{k=1}}^{\mathrm{K}}(\Delta\mathrm{S})_{\mathrm{kk}} = 0 \tag{2.54}$$

Since there is no electron gain or loss in the system, ΔS is zero. Performing an unitary similarity transformation on Δ provides the eigenvalues of Δ in the diagonal matrix (δ).

$$\exists\, \mathrm{U} \mid \delta = \mathrm{U}^{\dagger}\Delta\mathrm{U};\, (\delta)_{\mathrm{ij}} = 0 \quad \forall \quad \mathrm{i} \neq \mathrm{J} \tag{2.55}$$

Detachment/attachment orbitals [73] can be obtained by the diagonalizing the Δ matrix. Eigenvalues of Δ can be positive or negative. Two diagonal matrices, σ_- and σ_+, whose components are functions of those δ can be defined from the diagonalized matrix.

$$(\sigma_{\pm})_{kj} = \tfrac{1}{2}\left(\sqrt{(\delta)_{\mathrm{kk}}} \pm (\delta)_{\mathrm{kk}}\right) x\, \delta_{kj} \mid \delta = \textstyle\sum_{\omega=+,-}\omega\sigma_w \tag{2.56}$$

where $(\delta)_{kk}$ is a component of δ matrix and δ_{kj} is the Kronecker delta function. Δ's eigenvalues splitted in the two arrays by σ function. σ_+ contains only positiv values from the δ diagonal and zeros; while σ_- contains absolute values of negative δ values and sets non-negative ones to zero. Backtransforming δ, σ_- and σ_+ gives

$$\left.\begin{array}{r}\Delta = \mathrm{U}\delta\mathrm{U}^{\dagger} \\ \Gamma = \mathrm{U}\sigma_{-}\,\mathrm{U}^{\dagger} \\ \Lambda = \mathrm{U}\sigma_{+}\,\mathrm{U}^{\dagger}\end{array}\right\} \Rightarrow\ \Delta = \Lambda - \Gamma \qquad (2.57)$$

The two newly obtained matrices are the detachment Γ and attachment Λ density matrices, and are expressed in the space of the K atomic orbitals φ_μ. Because of the no electron is lost during the excitation process, we can see that

$$\sum_{\mu=1}^{K}(\Gamma \mathrm{S})_{\mu\mu} = \sum_{\mu=1}^{K}(\Lambda \mathrm{S})_{\mu\mu} \qquad (2.58)$$

However, related detachment/attachment densities can be defined in the real 3D space (ξ_1, ξ_2, ξ_3 are the three spatial coordinates)

$$\varrho_\tau(\xi_1\xi_2\xi_3) = \sum_{\mu=1}^{K}\sum_{\upsilon=1}^{K}(\tau)_{\mu\upsilon}\varphi_\mu(\xi_1\xi_2\xi_3)\varphi_\upsilon^*(\xi_1\xi_2\xi_3) \qquad (2.59)$$

$$\tau \equiv \Gamma, \Lambda \qquad (2.60)$$

Spatial distribution of the electronic density removed (detachment) from the ground state and reorganized (attachment) in the excited state during transition represented by Equation 2.59 and 2.60. Detached/attached charge ϑ_τ can be defined as

$$\vartheta = \int_{\mathbb{R}} d\xi_1 \int_{\mathbb{R}} d\xi_2 \int_{\mathbb{R}} d\xi_3\, \varrho_\tau(\xi_1\xi_2\xi_3) \equiv \int_{\mathbb{R}^3} d^3\xi_{\varrho_\tau}(\xi) \qquad (2.61)$$

$$\tau \equiv \Gamma, \Lambda \qquad (2.62)$$

Now, the dimensionless ϕ_S index as the overlap between the attachment and detachment densities can be defined as

$$\phi_s = \vartheta^{-1} \int_{\mathbb{R}^3} d^3\xi \sqrt{\varrho_\Gamma(\xi)\varrho_\Lambda(\xi)} \tag{2.63}$$

$$\vartheta \equiv \frac{1}{2}\left[\int_{\mathbb{R}^3} d^3\xi \sum_{\tau=\Gamma,\Lambda} \varrho_\tau(\xi)\right] \quad \phi_s \epsilon\ [0;1] \tag{2.64}$$

The ϕ_S index, that depends on the charge-transfer character of the electronic transition, ranges from 0 to 1. ϕ_S index can be equal to 0 if there is no overlap between detachment and attachment densities, and equal to 1 in an extreme case, where there is no electronic density fluctuation between ground and excited states. One may consider that a tridimensional integration grid surrounding the chromophore will integrate the detachment/attachment densities over the delimited volume Ω as depicted in Figure 4.2.

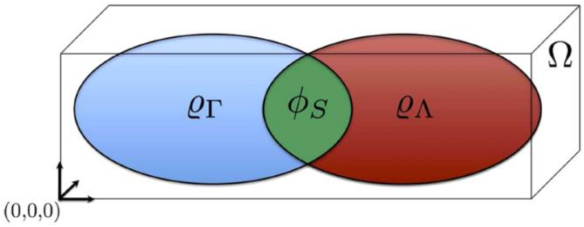

Figure 4.2. Graphical depiction of the ϕ_S descriptor as the overlap between detachment and attachment densities.

4.2.3 Computational Procedure

Both ground and excited states geometries of the molecules have been optimized at the B3LYP/6-31G* level of theory. Several hybrid, double hybrid, and long range corrected DFT functionals have been chosen to compute the excited state properties of the optimized structures. More in detail, global hybrid functionals use variable amount of pure Hartree-Fock [74] (HF) exchange to correct to the usual underestimation of charge transfer (CT) excitation energies. Among these, M06-2X [75], B3LYP [76, 77], and MPW1K [78] are the ones we have selected here. Long-range corrected functionals, on the other hand, including a higher fraction of exact HF exchange on a distance dependent way (i.e. at long separations), should in principle provide a more flexible correction to the above discussed limitations of DFT in the treatment of the CT states. Here we test the ωB97XD [79] approaches. Finally, we shall also evaluate the performances of two double-hybrid functionals [80], mPW2PLYP [81] and B2PLYP [82], which combining HF exchange and perturbative second-order correlation, require a computational overhead compared to global hybrid and range-separated methods.

The 6-31G* basis set was used to model the excited states of the molecules of interest and solvent effects were taken into account using polarizable continuum methods (PCM) [83]. The effect of the basis set size and in particular of the inclusion of polarization and diffusion functions was checked by performing benchmark calculations with the 6-31+G** basis set. However, in line with previous findings [59, 84], the results are only negligibly affected by the basis set dimensions.

For the purpose of this benchmark, absorption spectra have been modeled considering vertical transitions from the ground state equilibrium geometry, on the other hand vertical transitions from the first excited state (S_1) optimized geometry have been taken into account to model emission (fluorescence), equilibrating the solvent to the excited state of interest. Apart from double hybrid functionals, all the calculations with the other functionals (including optimizations) were performed with the Gaussian09 software package.

The calculations with the P2BLYP and mPW2PLYP double-hybrid functionals were carried out with the ORCA 2.9.0 package [85]. The Tamm-Dancoff approximation (TDA) was employed for the excitation energies and, following the protocol of previous benchmark works[86], numerical thresholds higher than the default values were adopted (TightSCF, Grid6, NoFinalGrid). The “resolution-of-the-identity” (RI) and “chain-of-spheres” (COSX) techniques[87, 88] were exploited in combination with a def2-DZVP auxiliary basis set.

In order to properly quantify the CT character of the electronic transitions, a recently developed methodology was applied: the Φs[72, 73, 89] index describes quantitatively the photoinduced electronic charge density variation. Specifically, Φs describe the overlap between the electron density removed from the ground state (detachment density, $\varrho\Gamma$) and the rearranged density in the excited state (attachment density, $\varrho\Lambda$). The CT character can be then obtained from the overlap value, also for long-range transfers. Values close to 1 are representative of a high overlap between the two densities and therefore indicate a local transition; on the other hand values close to 0 describe a very small overlap, indicating a CT transition. *Φ*s values have been calculated using the locally developed NANCY_EX_2.0 software package.

In order to include dynamic effects, 20 initial conditions were generated by sampling from a Wigner distribution[90, 91] as implemented in the Newton-X program [92]. As input, vibrational frequencies and the corresponding normal mode vectors were given by a frequency calculation performed on the ground state optimized geometries (B3LYP/6-31G* level of theory) for absorption and on the S1 optimized geometry for emission. Dynamic resolved spectra are than considered as the union of the vertical transitions calculated for each snapshot, both for absorption and for emission. In order to reproduce the experimentally resolved band shape, vertical transitions have been also convoluted with Gaussian functions of fixed width at half length (FWHL).

Finally, TPA cross sections have been calculated at the TD-DFT level as quadratic residue of the linear response, as implemented by Rizzo and coworkers [93]. Calculations have been performed using the DALTON2016 code [94] solvent effects have been taken into account using linear response PCM. In order to assure a direct comparison with the experimental cross section values are given in Göppert-Mayer (GM) units (10^{-50} cm^4 $photon^{-1}$).

4.3. Results and Discussion

Here we discuss the results of the benchmark calculations performed to assess the performance of the different functionals in reproducing the values of vertical excitation energies. The TD-DFT excitation energies have been checked both against high level ab-initio calculations and experimental data. The best functional will subsequently be used to treat the dynamical effects sampling the Wigner distribution [71]. In Table 4.1 we report the performance of different classes of functionals, also including double hybrid, in calculating the vertical excitation energies against the CAS-PT2 results [95].

Table 4.1. Benchmark calculations for absorption. λ_{Max} values are given in nm and, values in parenthesis represent the excitation energies given in eV.

	mPW2PLYP/6-31G*	B2PLYP/6-31G*	ωB97XD/6-31G*	CAS-PT2/6-31G*
A1	390(3.18)	397(3.12)	383(3.24)	404(3.07)
A2	426(2.91)	433(2.87)	419(2.96)	
A3			442(2.80)	
B1	360(3.44)	367(3.38)	344(3.60)	361(3.43)
B2	356(3.49)	363(3.42)	348(3.56)	
B3	361(3.44)	371(3.35)	338(3.67)	
C1		383(3.24)	362(3.42)	

Indeed, one may see that a global agreement holds with differences that are generally less than 0.1 eV. Remarkably, the long-range corrected ωB97XD functional provides results that have the same quality of the way more expensive double-hybrid or multiconfigurational methods. Even if we focus on the brighter S_1 state, it is remarkable that the same good agreement holds for the S_2 state, the difference between CAS-PT2 and TD-DFT results being of the order of 0.05 eV.

In Table 4.2, the effect of the solvent (dichloromethane) was also tested, using PCM methods and also compared to experimental results. If we compare Table 4.1 and Table 4.2 results it appears evident that compounds belonging to family A appear to be moderately affected by the solvent as the number of thiophene rings increases; this is possibly due to the fact that thiophene is known for having relatively high polarizabilities resulting more sensitive to the solvent induced field. Families B and C show, on the other hand, only negligible deviations between vacuum and dichloromethane. The performance of linear response PCM over state specific calculations was also checked in the case of ωB97XD, indeed state-specific implicit model can have important effects when in the presence of charge transfer or for excited states having high quadrupolar moments, as it is the case for the bright $S_{1.}$ However, in the present case for A1 and B1 state-specific solvation only shifts the vertical excitation energy of 0.07 and 0.09 eV, respectively. The same trend is also observed for the S_2 state.

The effects of the basis set size on the prediction of the excitation energies was also checked by comparing the 6-31G* results with those obtained with the 6-31+G** basis set, when the ωB97XD functional is employed (Table 4.2). It is evident that the inclusion of polarization and diffusion functions does not affect λ_{Max} values dramatically for all the families, the difference being of the order of 10^{-2} eV.

Concerning the effect of the different class of functionals, as one could expect, the deviation of the B3LYP excitation energies increases as the number of thiophene rings increases within Family A. The lack of the long range correction in the B3LYP functional, and hence the related overstabilization of charge transfer states, seems to be the reason of such misleading results. The λ_{max} values calculated with the M06-2X hybrid functional and the long-range corrected hybrid functional ωB97XD are similar to each other, the difference between the results of the two functionals not exceeding 0.01-0.02 eV. The results obtained with MPW1K are close to the M06-2X and ωB97XD results as well; however the former consistently has yielded slightly red-shifted λ_{max} values compared to the others.

Globally for family A it appears that M06-2X, MPW1K and B97XD give the overall lowest deviations from experimental values. When considering family B, once again B3LYP gives significantly lower excitation energies than CAS-PT2. Furthermore, experimentally, slight blue shift in λ_{max} has been observed in going from B1 to B3. Hybrid functionals M06-2X, MPW1K and the long-range corrected hybrid functional ωB97XD have reproduced this finding, both qualitatively and quantitatively yielding a B3 absorption maximum shifted of about 0.1 eV compared to B1. As was the case for the members of the A family, B3LYP appears to perform quite badly. Overall, long-range corrected functionals as well as M06-2X and MPW1K are able to satisfactorily reproduce the experimental trends. Finally in the case of the C1 molecule, all the functionals except B3LYP have yielded similar results for the calculation of vertical excitation energies with maximum deviations not exceeding 0.2 eV from experimental values.

The hybrid functionals M06-2X, B3LYP, MPW1K and the long-range corrected hybrid functional ωB97XD have been used for the calculations of emission spectra (Table 4.3). In this case, experimental and calculated values show larger deviation than for absorption, however differences are still acceptable with errors of about 0.2 eV, the trends inside the families being also correctly reproduced.

Table 4.2. Benchmark calculations and experimental results [38] for absorption including solvent effects. λ_{Max} values are given in nm and, values in parenthesis represent the excitation energies given in eV.

	B3LYP/ 6-31G*	M06-2X/ 6-31G*	MPW1K/ 6-31G*	ωB97XD/ 6-31G*	ωB97XD/ 6 -31+G**	Exp.
A1	458(2.71)	399(3.11)	407(3.05)	393(3.15)	399(3.11)	411(3.02)
A2	509(2.44)	439(2.82)	452(2.74)	432(2.87)	439(2.82)	449[a](2.76)
A3	553(2.24)	465(2.67)	484(2.56)	456(2.72)	464(2.67)	469(2.64)
B1	420(2.95)	358(3.46)	366(3.39)	351(3.53)	356(3.48)	373(3.23)
B2	414(2.99)	352(3.52)	361(3.43)	343(3.61)	338(3.67)	370(3.35)
B3	431(2.88)	351(3.52)	359(3.45)	342(3.62)	346(3.58)	360(3.44)
C1	448(2.77)	376(3.30)	388(3.19)	368(3.37)	372(3.33)	377(3.29)

Furthermore, as was the case for absorption spectra, the inclusion of polarization and diffuse functions in the basis set has only slight effects on the emission vertical transition energies. Coherently with the results for absorption spectra, the hybrid M06-2X and long range corrected hybrid ωB97XD functionals single out as the top performers in the simulation of emission spectra.

Taking into account all the previous results, we decided to use the ωB97XD/6-31G* level of theory for the calculations of absorption and emission spectra taking into account dynamic effects.

Table 4.3. Benchmark calculations and experimental results [38] for emission. λ_{Max} values are given in nm and, in parenthesis, in eV.

	B3LYP /6-31G*	M06-2X /6-31G*	MP1WK/ 6-31G*	ωB97XD /6-31G*	ωB97XD /6-31+G**	Exp.
A1	659(1.88)	445(2.79)	473(2.62)	434(2.86)	441(2.81)	452(2.74)
A2	580(2.14)	514(2.41)	528(2.35)	507(2.44)	518(2.39)	506(2.45)
A3	602(2.06)	525(2.36)	545(2.27)	516(2.40)	528(2.35)	537(2.31)
B1	583(2.13)	418(2.97)	438(2.83)	395(3.14)	399(3.11)	433(2.86)
B2	477(2.60)	390(3.18)	402(3.08)	379(3.27)	385(3.22)	419(2.96)
B3	646(1.92)	388(3.19)	404(3.06)	416(2.98)	425(2.92)	505(2.46)
C1	495(2.50)	418(2.97)	432(2.87)	408(3.04)	413(3.00)	410(3.02)

4.3.1 Excited States Topology and NTO

In the following figures, the occupied and virtual NTOs describing $S_0 \rightarrow S_1$, $S_0 \rightarrow S_2$ and $S_0 \rightarrow S_3$ (absorption) and $S_1 \rightarrow S_0$ (fluorescence) vertical transitions are shown, including excitation energy and oscillator strength (f). The calculations were performed at the ωB97XD/6-31G*//B3LYP/6-31G* level of theory, including DCM as solvent.

Table 4.4. Virtual and Occupied NTO's of A1

Absorption	Occupied	Virtual
$S_0 \rightarrow S_1$ Energy = 3.153 eV f = 1.3509	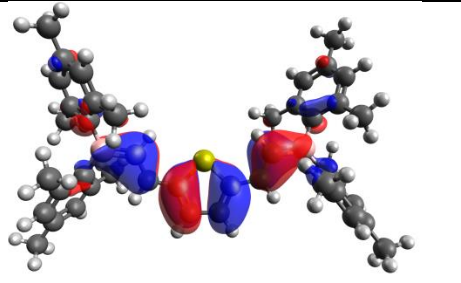	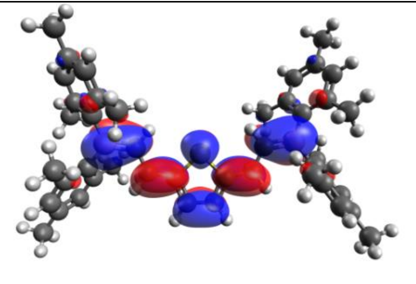
$S_0 \rightarrow S_2$ Energy = 3.898 eV f = 0.1589	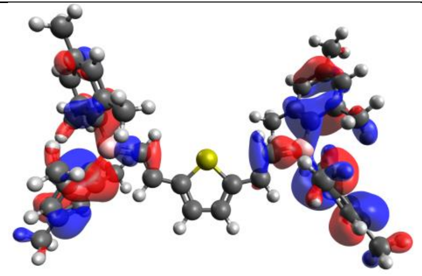	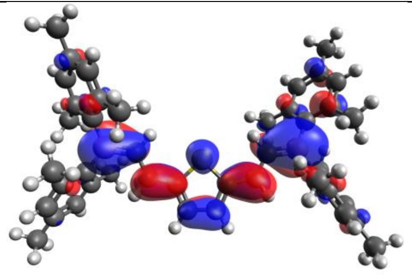

Table 4.4. Virtual and Occupied NTO's of A1

$S_0 \rightarrow S_3$ Energy = 3.898 eV f = 0.0140	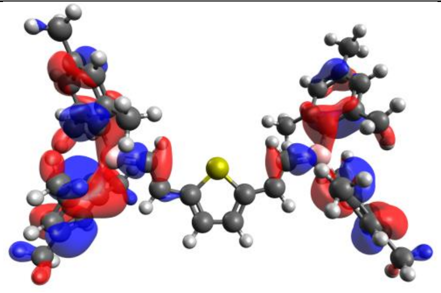	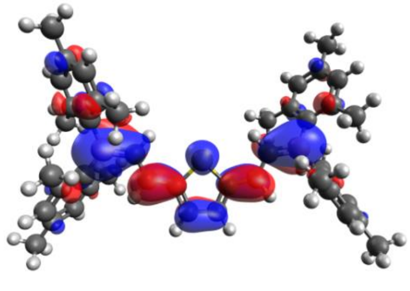
Emission		
$S_1 \rightarrow S_0$ Energy = 2.854 eV f = 1.2908	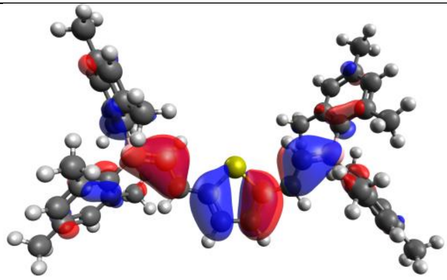	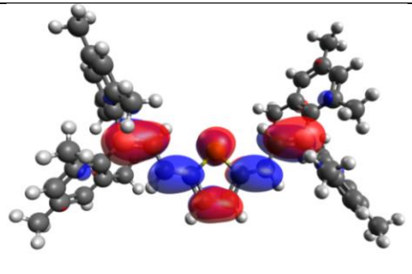

Table 4.5. Virtual and Occupied NTO's of A2

Absorption	Occupied	Virtual
$S_0 \rightarrow S_1$ Energy = 2.872 eV f = 1.9251	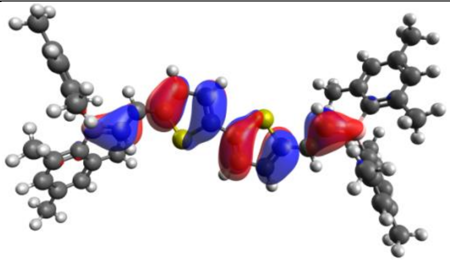	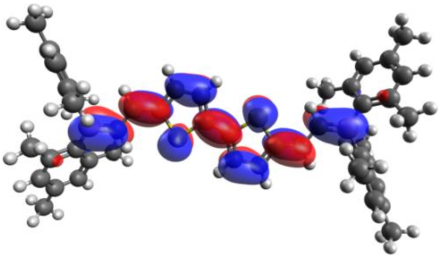
$S_0 \rightarrow S_2$ Energy = 3.818 eV f = 0.0014	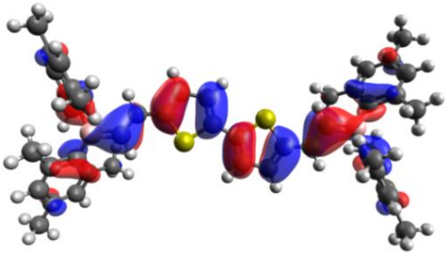	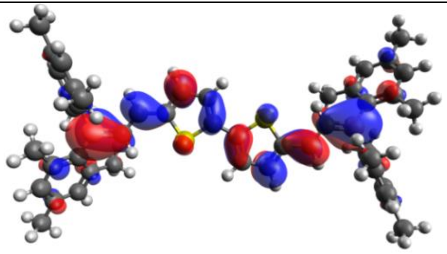
$S_0 \rightarrow S_3$ Energy = 3.929 eV f = 0.1677	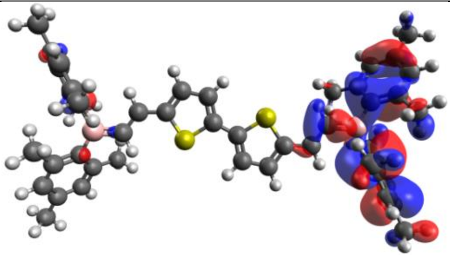	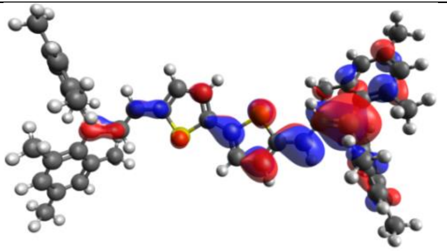
Emission		
$S_1 \rightarrow S_0$ Energy = 2.444 eV f = 1.8227	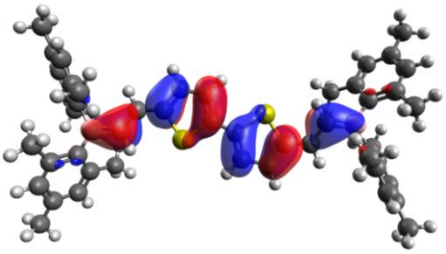	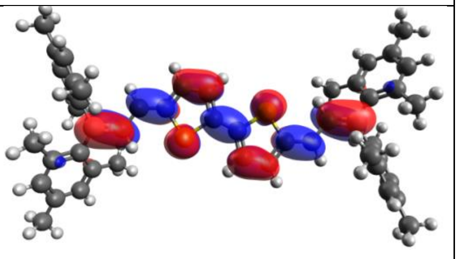

Table 4.6. Virtual and Occupied NTO's of A3.

Absorption	Occupied	Virtual
$S_0 \rightarrow S_1$ Energy = 2.721 eV f = 2.2777	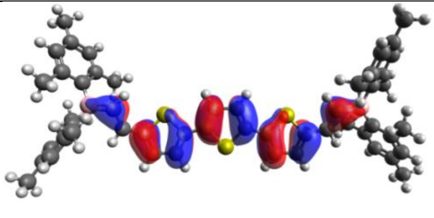	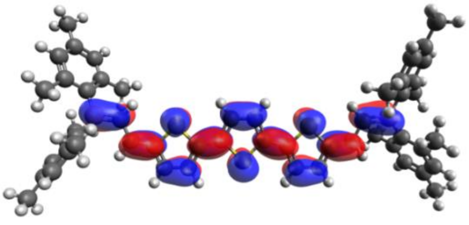

Table 4.6. Virtual and Occupied NTO's of A3.

$S_0 \rightarrow S_2$ Energy = 3.487 eV f = 0.1566	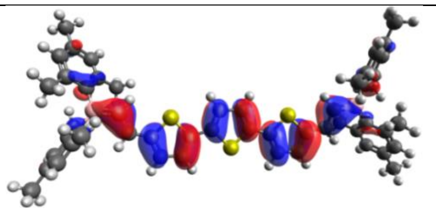	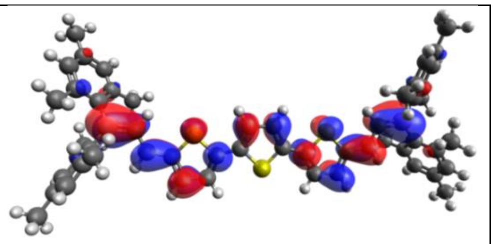
$S_0 \rightarrow S_3$ Energy = 3.940 eV f = 0.0209	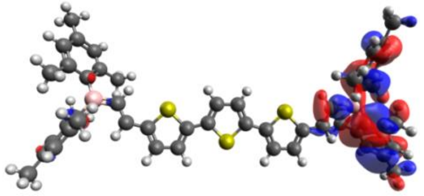	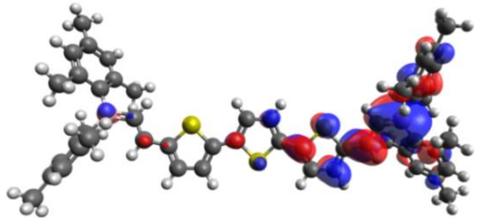
Emission		
$S_1 \rightarrow S_0$ Energy = 2.402 eV f = 2.2100	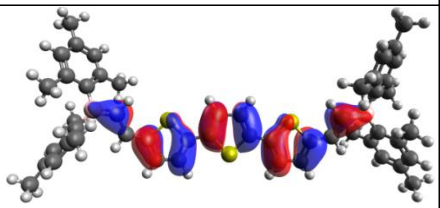	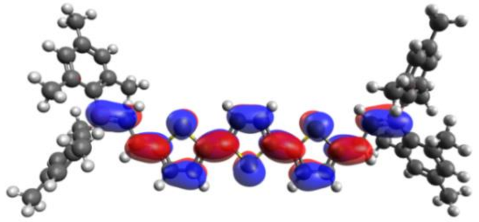

Table 4.7. Virtual and Occupied NTO's of B1.

Absorption	Occupied	Virtual
$S_0 \rightarrow S_1$ Energy = 3.533 eV f = 1.7717	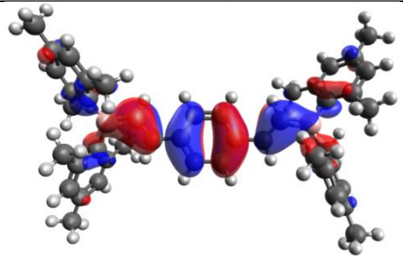	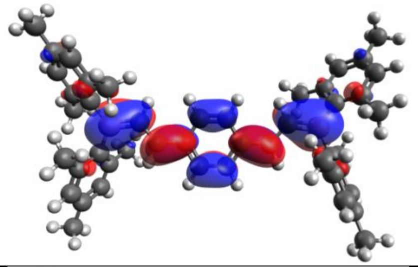
$S_0 \rightarrow S_2$ Energy = 3.971 eV f = 0.0120	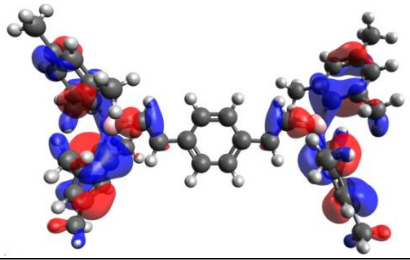	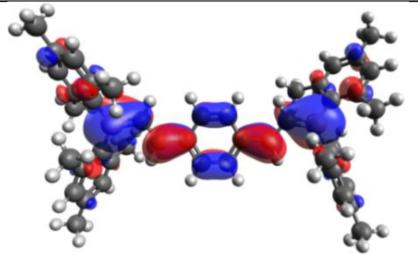

Table 4.7. Virtual and Occupied NTO's of B1.

$S_0 \rightarrow S_3$ Energy = 3.973 eV f = 0.1889	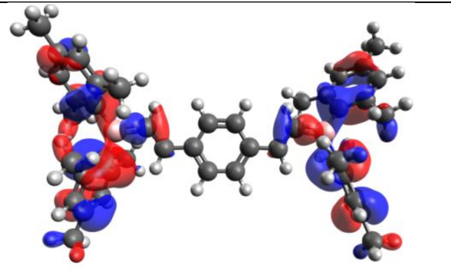	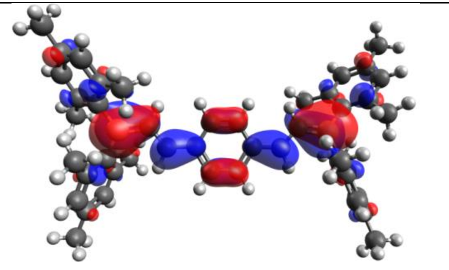
Emission		
$S_1 \rightarrow S_0$ Energy = 3.136 eV f = 0.5865	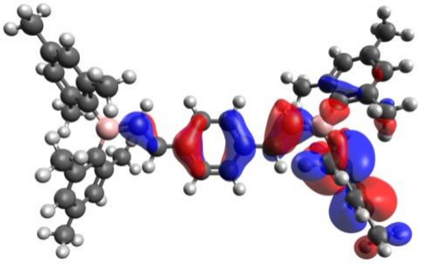	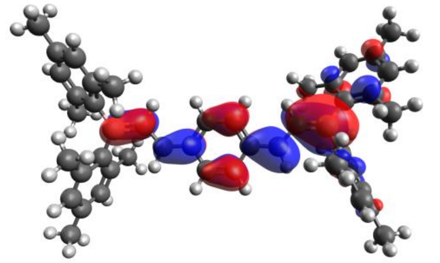

Table 4.8. Virtual and Occupied NTO's of B2.

Absorption	Occupied	Virtual
$S_0 \rightarrow S_1$ Energy = 3.611 eV f = 2.4624	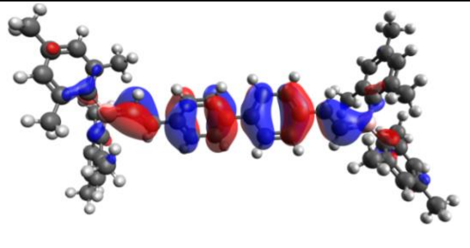	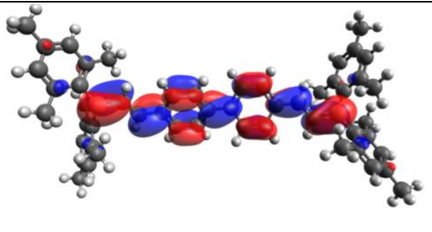
$S_0 \rightarrow S_2$ Energy = 4.023 eV f = 0.0395	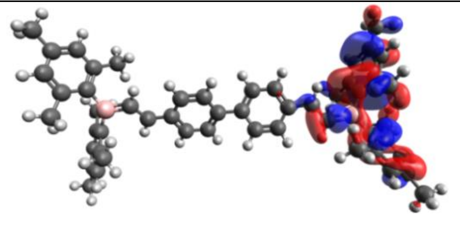	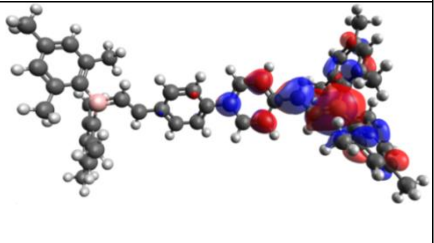
$S_0 \rightarrow S_3$ Energy = 4.027 eV f = 0.1827	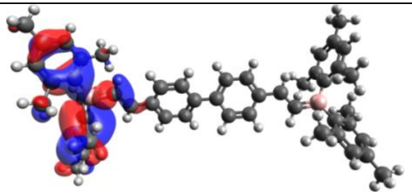	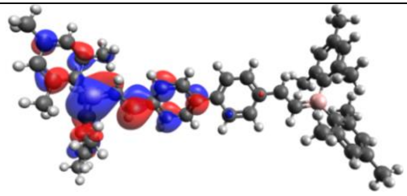
Emission		
$S_1 \rightarrow S_0$ Energy = 3.269 eV f = 2.3690	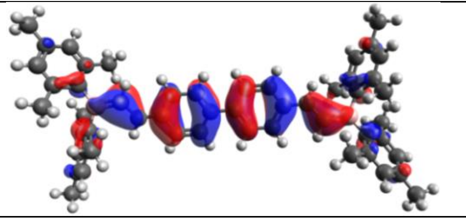	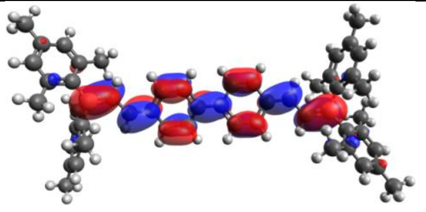

Table 4.9. Virtual and Occupied NTO’s of B3

Absorption	Occupied	Virtual
$S_0 \rightarrow S_1$ Energy = 3.618 eV f = 1.5657	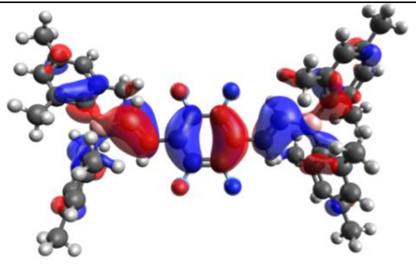	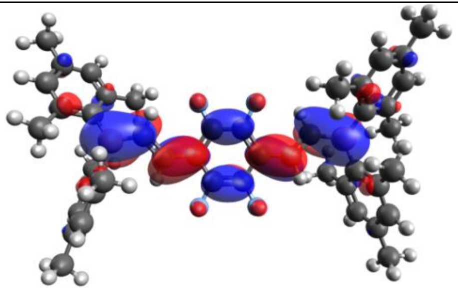
$S_0 \rightarrow S_2$ Energy = 3.824 eV f = 0.0198	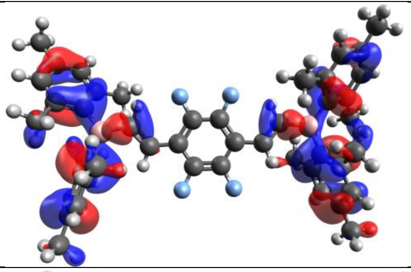	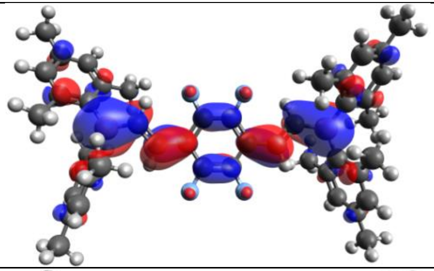
$S_0 \rightarrow S_3$ Energy = 3.825 eV f = 0.2004	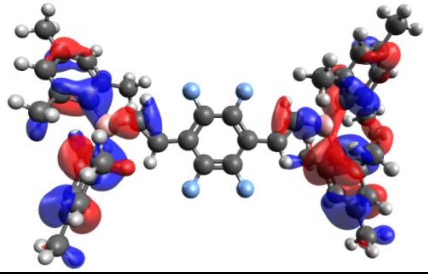	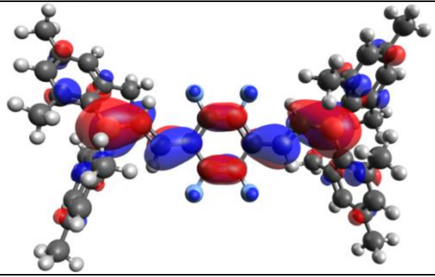
Emission		
$S_1 \rightarrow S_0$ Energy = 2.980 eV f = 0.0622	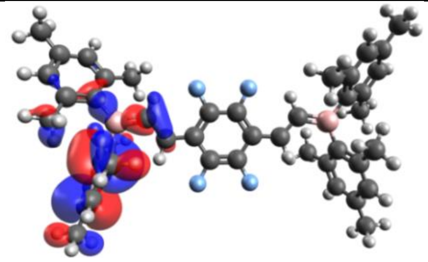	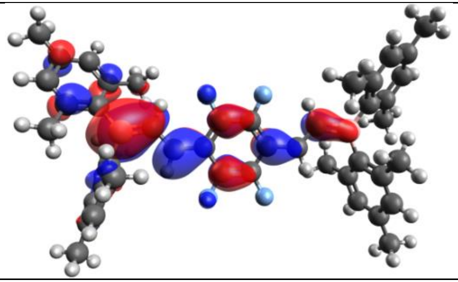

Table 4.10. Virtual and Occupied NTO’s of C1.

Absorption	Occupied	Virtual
$S_0 \rightarrow S_1$ Energy = 3.372 eV f = 2.9023	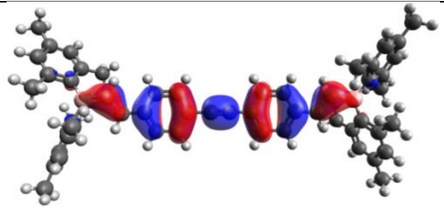	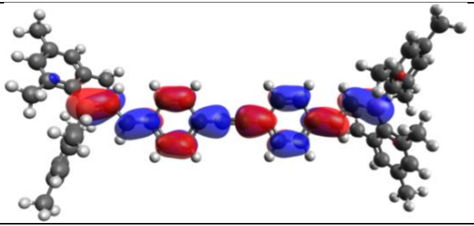

Table 4.10. Virtual and Occupied NTO's of C1

$S_0 \rightarrow S_2$ Energy = 3.938 eV f = 0.0504	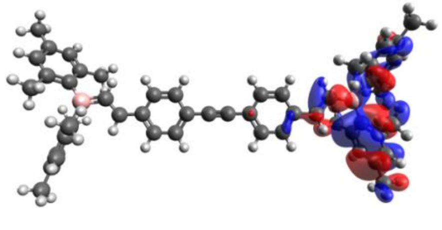	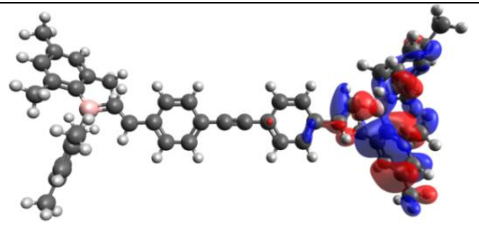
$S_0 \rightarrow S_3$ Energy = 3.963 eV f = 0.0155	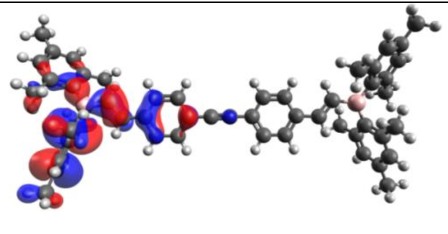	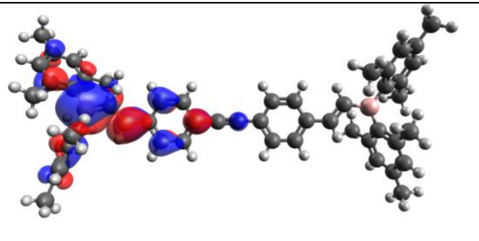
Emission		
$S_1 \rightarrow S_0$ Energy = 3.038 eV f = 2.8390	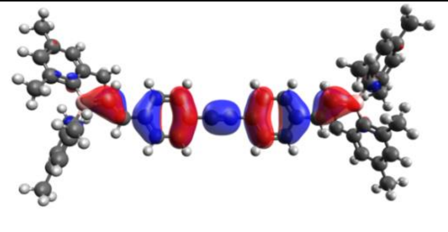	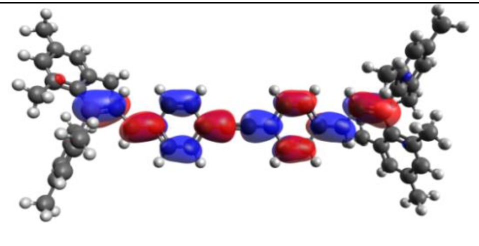

NTOs describing the $S_0 \rightarrow S_1$ vertical transition for the all members of each family are reported in Table 4.4 to Table 4.10 , while Φs values are reported in Table 4.11. We remind that low Φs value indicates the presence of a CT transition. The first excited state of all the molecules is mainly local and can be easily assigned as a π-π* transition mostly localized on the conjugated bridge. However, the participation of the boron moiety is non negligible. The value of the Φs index strongly decreases for the second or third excited state indicating the presence of a real CT state. Low lying CT is usually directed from one of the boron moiety toward the bridge arene center. As a consequence, and because of symmetry reasons, one may notice the presence of two quasi-degenerate transitions ($S_0 \rightarrow S_2$ and $S_0 \rightarrow S_3$) involving the right or left boron moiety in the CT.

In the case of the A family the first member's second excited state (S_2) is already clearly of CT nature, while adding one more thiophene ring changes the ordering of the state inducing a second low-lying local excitation. The same is true for the A3 molecule, in which however the interpretation of the Φs values alone is more complicated due to the increased length of the bridge system. The same tendencies are pretty well reproduced also in the case of emission, i.e. considering vertical transitions calculated from the first excited state equilibrium geometries, $S_1 \rightarrow S_0$.

The same general consideration can be drawn for the Family B; indeed also in this case the second and third states (S_2 and S_3) are of clear CT character. However, upon excited state geometry optimization one can see a clear modification of the excited state nature, especially evident for the B3 compound for which the S_1 state at its equilibrium geometry is of clear CT character. This larger stabilization of the CT state can certainly be ascribed to the presence of electron attractor atoms (fluorine) on the phenyl bridge, i.e. on the region where the electrons are accumulated.

Finally, C1 has shown similar CT behavior as seen in the other families, with once again a lowest lying local excited state (S_1) at Franck−Condon, followed by two CT states (S_2 and S_3). However, when compared to B2, which contains only two phenyl rings in the arene center, C1 has shown less CT character; hence the introduction of sp carbons between two phenyl rings induces a significant decrease in the CT.

Table 4.11. Calculated (ωB97XD/6-31G*//B3LYP/6-31G*) Φs for absorption (Φ_{ab}) and emission (Φ_{em}) values of the singlets

Transition	$S_0 \leftrightarrow S_1$		$S_0 \rightarrow S_2$	$S_0 \rightarrow S_3$
Molecule	Φ_{ab}	Φ_{em}	Φ_{ab}	Φ_{ab}
A1	0.87	0.88	0.29	0.26
A2	0.90	0.84	0.78	0.32
A3	0.61	0.92	0.53	0.57
B1	0.87	0.56	0.34	0.33
B2	0.88	0.88	0.38	0.39
B3	0.82	0.27	0.38	0.36
C1	0.93	0.93	0.44	0.58

4.3.2 Dynamic Effects on Optical Properties

The absorption and emission spectra calculated convoluting over snapshots obtained from the Wigner distribution are shown in Figures 4.10 (absorption) and Figure 4.11 (emission), while the calculated band maxima are listed in Table 4.12 along with the experimental results. Note that in all the cases, and due to the difference in oscillator strength, the spectra are dominated by the brighter transition to S_1 the band shape, and the secondary peaks being due only to the coupling with the vibrational degrees of freedom. The included dynamic effects increase the agreement with the experimental results for all the studied families of arenes, as compared to the static TD-DFT calculations.

For the A2 molecule only experimental results in toluene solution are available, hence the spectrum has been reproduced in this solvent. DCM and toluene solvents have different characteristics with dipole moments of 1.6 D and 0.36 D, respectively. Hence, in order to assess the effects of non-polar and polar solvent on our calculations A1, A2, B1 and B2 dynamics absorption spectra have been simulated using both solvents, modeled by PCM, on top of snapshots extracted from the Wigner distribution. The corresponding results are reported in Table 4.12, where it is evident that λ_{max} have not been significantly affected by the different environments, hence allowing for a comparison with the available experimental results. It is remarkable that also the general band shapes obtained from our sampling correctly reproduce the experimental ones, hence allowing a good reproduction of the main vibrational coupling effects.

Table 4.12. Calculated Wigner Distribution Results in toluene and DCM for absorption at ωB97XD/6-31G*//B3LYP/6-31G*

Molecule	λ_{Ab} in Toluene	λ_{Ab} in DCM
A1	395(3.14)	395(3.14)
A2	450(2.76)	450(2.76)
B1	375(3.31)	375(3.31)
B2	369(3.36)	370(3.35)

All molecules have shown their λ_{Max} in visible and near-UV regions both for absorption and emission. Dynamic effects sampled by the Wigner distribution have been crucial in particular in the case of molecules having out-of-plane low-frequency high-amplitude vibrational normal modes. Indeed, the former vibrations weaken the conjugated pattern hence influencing differently the energy of ground and excited states. Compared to the static calculations A2 and A3 have shown red-shift (0.10 and 0.07 eV, respectively) and the inclusion of vibrational effects has allowed to almost perfectly recover the experimental results (only 1 nm difference). On the other hand the absorption maximum for the A1 molecule, characterized by a much shorter bridge, has been red-shifted by only 0.01 eV. C1 is also only slightly affected by dynamic effects as well with a shift of less than 0.1 eV. This fact should certainly be ascribed to the rigidity imposed to the molecule by the bridging triple bond. Similar band shapes have been obtained for A1 and A3 (Figure 4.10); both molecules have shown a shoulder, due to vibrational effects, after the intense λ_{Max}. A1 has shown its shoulder around 390 nm, and it was more evident compared to the shoulder of A2, which can be seen around 490 nm. A less intense peak has been observed in the spectrum of A2 at 406 nm. However, that peak is weak, compared to more intense λ_{Max} observed at 450nm.

Family B has shown significant improvement in the terms of λ_{Max} compared to the static TD-DFT calculations, due to low frequency vibrations of the phenyl ring. All members of the family B have shown a red-shift of 24-28 nm (0.1 eV) after the introduction of dynamic effects. λ_{Max} of B2 is 343 nm by static TD-DFT calculation; with the inclusion of dynamic effects the emission maximum has been red-shifted to 370 nm, which happens to perfectly match the experimental value also.

The different substitutions in the arene center have not shown any major effect for the λ_{Max} within the family B. However, the band shape is quite peculiar of each member; in particular the B1 molecule shows the stronger vibronic effect with a well-resolved maximum at around 420 nm, while B2 only shows shoulders. Finally in the case of the B3 molecule the inclusion of fluorine atoms on the bridge shifts the vibronic shoulder at shorter wavelengths than the absorption maximum.

On the other hand and once again most probably due to the increased rigidity C1 shows a rather symmetric spectrum in which vibronic effects are absolutely negligible.

Also in the case of emission (Table 4.13) dynamic effects proved extremely important for families A and B. Family A has shown remarkable red-shifts of 0.16 and 0.12 eV for A1 and A3, respectively compared to the static picture. Family B has shown red-shifted λ_{Max} values compared to the static TD-DFT calculations of 0.34 and 0.04 eV for B1 and B2, respectively. On the other hand, a very important 0.56 eV (62 nm) red-shift has been observed for the B3. This should also be correlated to the fact that upon geometry optimization the first excited state has a marked CT character. In particular the mesityl group bearing the hole density is involved in a very low-frequency normal mode (14 cm^{-1}). On the other hand and as was already the case for absorption, a relatively small shift of about 0.15 eV is observed in the case of the C1 molecule, hence once again, because of the rigid structure imposed by the triple bond dynamic effects are only marginal.

As far as the band shapes are involved (Figure 4.11) we may observe a rather asymmetric band, with a long tail extending to long wavelengths, being this feature almost universal in the case of fluorescence spectra. Furthermore, we may evidence the appearance of a number of shoulders or secondary maxima in the vibrationally resolved spectra that is also the signature of important vibrational effects. However, those characteristics are not always easily recognizable in the experimental spectra also because of a relatively low resolution.

Overall, it has been proven that dynamic effects may be crucial to reproduce the band shapes, as well as absorption and emission maxima, especially for highly conjugated systems or CT states. It also appears that Wigner distribution is an easy and straightforward way to include those effects with only a moderate computational overload.

Table 4.13. Experimental [38] and calculated (ωB97XD/6-31G*//B3LYP/6-31G*) λ_{Max} in DCM, via Wigner procedure. Corresponding absorption and emission maxima are given in nm and, in parenthesis, in eV.

	λ_{ab}	$\lambda_{ab\text{-}Exp.}$	λ_{em}	$\lambda_{em\text{-}Exp}$
A1	395(3.14)	411(3.02)	453(2.74)	452(2.74)
A2	450[a](2.76)	449[a](2.76)	506(2.45)	506(2.45)
A3	470(2.64)	469(2.64)	554(2.24)	537(2.31)
B1	375(3.31)	373(3.23)	422(2.81)	433(2.86)
B2	370(3.35)	370(3.35)	384(3.23)	419(2.96)

Table 4.13. Experimental [38] and calculated (ωB97XD/6-31G*//B3LYP/6-31G*) λ_{Max} in DCM, via Wigner procedure. Corresponding absorption and emission maxima are given in nm and, in parenthesis, in eV. (cont.)

B3	370(3.35)	360(3.44)	488(2.54)	505(2.46)
C1	380(3.26)	377(3.29)	428(2.90)	410(3.02)

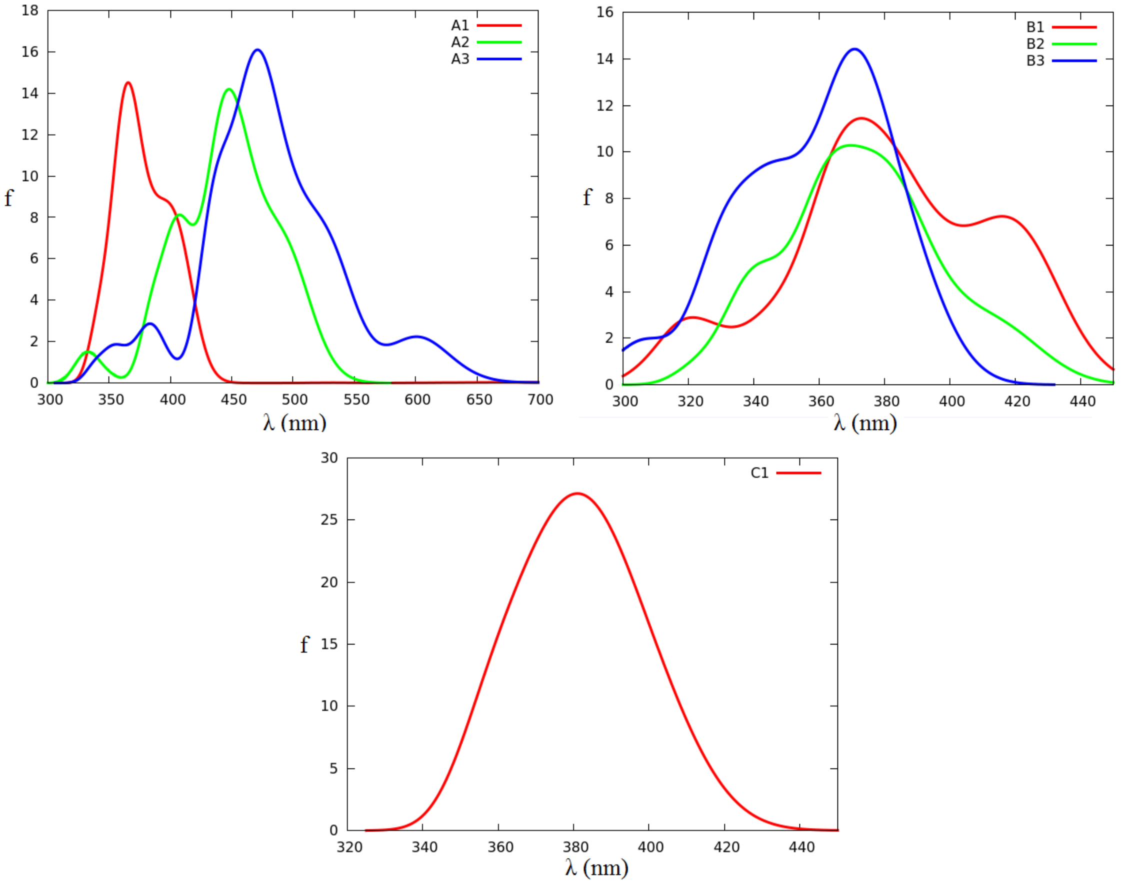

Figure 4.10. Results of the Wigner distribution calculations for absorption spectra of the each family. All the vertical transitions have been convoluted with Gaussian functions of fixed width at half-length of 0.2 eV

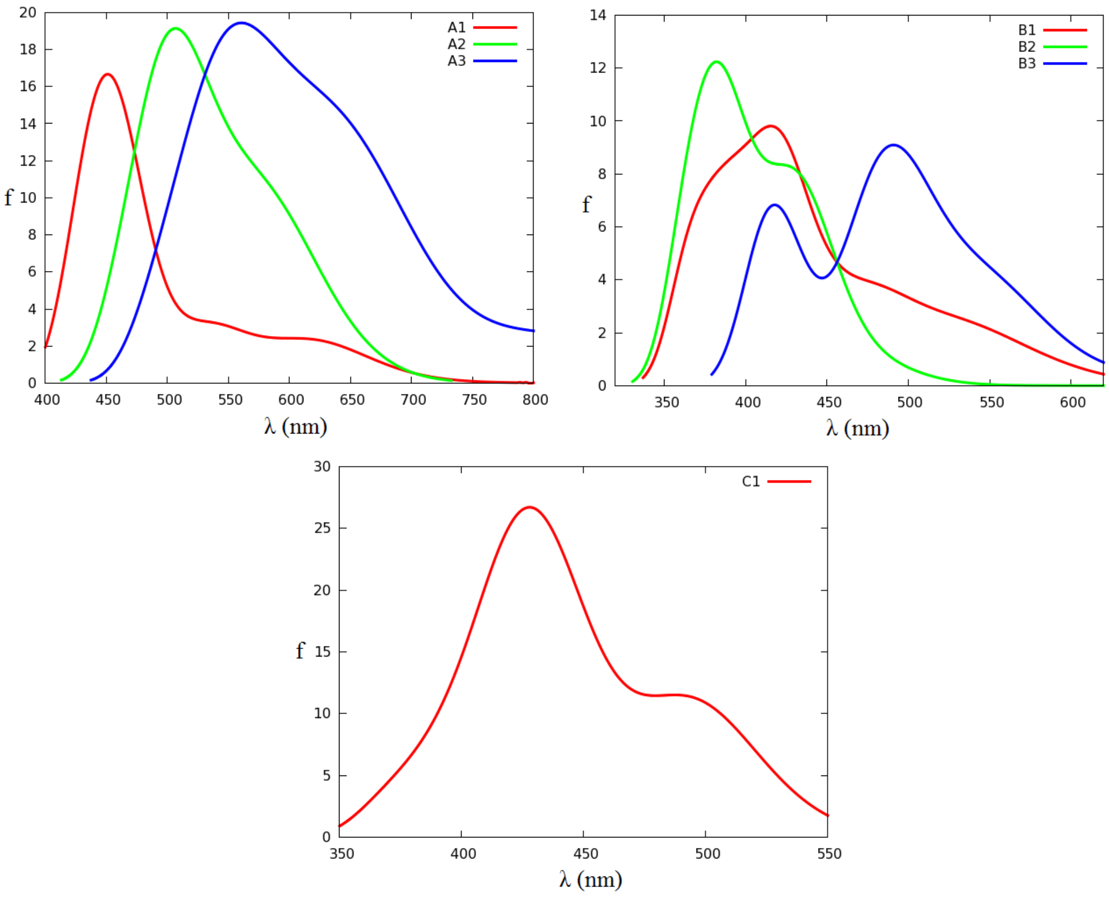

Figure 4.11. Results of the Wigner distribution calculations for emission spectra of the B and C families. All the vertical transitions have been convoluted with Gaussian functions of fixed width at half length of 0.3 eV

4.3.3 Two-photon absorption

Two photon absorption cross sections are shown in Table 4.14. Coherently with experimental data the different molecules appear to be red or infra-red TPA absorbers, hence could be potentially used in optical applications involving long wavelength excitations. However, and differently from one photon absorption, the S_2 state is always the optically brightest one. This aspect was also hypothesized by experimental measurement, since the TPA maximum happens at wavelengths shorter than twice the one-photon absorption maximum. Concerning TPA cross-section, family A singles out as the most promising one. Indeed cross-sections are much higher than the ones for the other families. As expected, the lengthening of the thiophene bridge has a very strong and non-linear effect: indeed in the case of A3 (three thiophene) one reaches very high cross sections of more than 1000 GM. Even if the experimental data have a very low resolution and hence are burden with a rather large uncertainty, a good agreement with experimental TPA cross sections is also observed. Indeed in the case of A3 the experimental TPA cross section is around 1500 GM to be compared with the calculated 1010 GM.

On the other hand, phenyl containing molecules (family B) have shown rather weak TPA cross-sections compared to the thiophene containing molecules, also the lengthening of the conjugated bridge has virtually no effect on the TPA cross section, nor has the inclusion of fluorine atoms. Indeed for all the B family molecules, TPA cross section values of around 35 GM are observed. Remarkably enough, a good agreement with the experimental data is found both in terms of maximum TPA and cross-section reported to be around 25 GM.

Similarly, the inclusion of the bridged triple bond (C1) is not beneficial and does not increase the cross section above the 40 GM level. Hence it appears evident that the inclusion of the thiophene bridge is by far the most beneficial way to increase the TPA efficiency of the studied systems. Indeed, already the addition of the second thiophene ring (A2) implies an increase in the cross section of about one third, while upon the addition of the third ring (A3) an increase of two orders of magnitude is observed. This fact is certainly due to the remarkable polarization of the thiophene units that are extremely beneficial to increase the TPA cross section. The effect of the bridge seems to dominate over all the other factors, and the presence of boron does not seem crucial. This aspect is also confirmed by calculating TPA cross-sections for a model α-ω-vinyl terminated terthiophene, corresponding to the thiophene bridge of the A3 molecule. Indeed the former gives a TPA cross-section of 1090 GM for absorption at 784 nm.

Table 4.14. Calculated two photon absorption cross-sections and absorption wavelengths.

Molecule	λ_{Max} (nm)	Φ (GM)
A1	780	1.27
	661	46.27
A2	855	1.70

Table 4.14. Calculated two photon absorption cross-sections and absorption wavelengths. (cont.)

	657	64.32
A3	905	2.45
	700	1010.00
B1	702	0.26
	646	37.52
B2	636	0.28
	691	34.78
B3	692	0.50
	674	35.08
C1	740	0.23
	649	40.7

4.4 Conclusion

Ground and excited state properties of a series of oligomers including three coordinated boron and bis(E-dimesitylborylethenyl) arenes have been investigated computationally. Extended benchmark test, based on the use of double-hybrid functionals and CAS-PT2 calculations, has unraveled the effects induced by the choice of the different functionals and particularly the importance of the non-local exchange as well as long-range correction to recover the correct excitation energies. In fact, our results indicate that the hybrid M06-2X and MPW1K functionals along with the long-range corrected ωB97XD approach are the best performing methods for the prediction of both the absorption and emission properties.

The influence of dynamic and vibrational effects on absorption and emission spectra have been taken into account by exploring the conformational space of the ground and first excited state, respectively via Wigner distribution. This straightforward strategy allowed us to qualitatively and quantitatively reproduce the red-shift induced in particular by the low-frequency, high-amplitude out-of-plane normal modes that break the conjugation pattern differentially between ground and excited states.

The relations between the structure and the optical properties of the different arenes have been clearly identified and rationalized. Although all the systems have shown emission in the visible region, only A2 and A3 presented their λ_{max} of absorption in visible region, as a consequence of the addition of extra thiophene rings. Moreover, NTO analysis of the excited states has shown that while the first optically bright excited state is local, the main charge transfer takes place for the second and third excited states of the molecules. As far as non-linear optical properties are concerned, it has been shown that all the systems may potentially act as infra-red TPA absorbers, the bright state in this case being the second one. However, thiophene containing oligomers show extremely good and promising TPA cross-sections. Most notably the effect of the addition of thiophene rings on TPA cross-sections is not linear and indeed A3 has shown remarkable intensity TPA reaching 1010 GM at 700 nm. It appears evident that, especially for the thiophene containing systems, one may envisage the possibility of exploitation the in different applications ranging from organic semiconductors to light-emitting devices. Indeed, TPA-absorbing molecular devices or sensors will be activated by red or infrared light-pulses, hence will cover a not yet widely exploited spectral windows. Furthermore, the non-linear properties of TPA will allow to precisely activate the device with a much higher spatial resolution.

We have clearly demonstrated the ability of our multiscale protocol to provide a complete description of the different optical properties of complex systems in realistic environment, taking into account an equal footing electronic and vibrational effects. In a future work we plan to extend the study of these promising systems, in particular taking into account their photostability, and hence analyzing the possible photodegradation pathways available in the presence of oxygen and water. As such, a first study will be devoted to the possible activation of singlet oxygen, via the preliminary population of the chromophores' triplet manifolds, which is known to be responsible of many oxidative degradation processes in organic systems.

5. UNDERSTANDING THE IMPACT OF THIOPHENE/FURAN SUBSTITUTION TO INTRINSIC CHARGE-CARRIER MOBILITY

5.1. Introduction

Hendsbee *et al.* [96] have synthesized bifuran (bi-F) and bithiophene (bi-T) derivatives as shown in Figure 5.1. Despite the predicted minimal change in electronic and optical properties, along with the better sustainability, an unusual loss of electron mobility of bi-F and as well as an increased hole mobility had been reported. Nguyen *et al.* [97] have also reported the loss of electron mobility and the slightly increasing hole mobility in substitution of furan for thiophene. Charge transfer in the crystal structure can occur via hopping type mechanism or band type mechanism [98]. Most of the time π-conjugated oligomers transport their charge via hopping type mechanism at high temperatures. This type of charge transfer depends on the packing of the molecules, orientations of the molecules with respect to other and their regioregularities [99]. However, correlation between charge transfer and packing arrangement, molecular structure and natural disorder in the self-assembled crystals yet has to be fully explained [100]. Despite the proposed methodologies[101–104] to understand structure and charge transfer behaviors, the link between atomistic properties and overall device characteristics are still unclear. Consequently, limited understanding of bulk properties of the materials at the atomistic level slow down the theoretical progress for finding better organic semiconductors.

It is well known that the substitution of even one atom can affect the crystal structure dramatically [105]. Although, they have different atoms on the central block of the molecule, in solid state packing of these two derivatives are quite similar to each other, with similar orientations of the neighboring molecule’s backbones to each other and the centroid to centroid distance between adjacent molecules. Solely, the positions of the side chains with respect to the backbone are the only significant differences that have been observed in solid state packing.

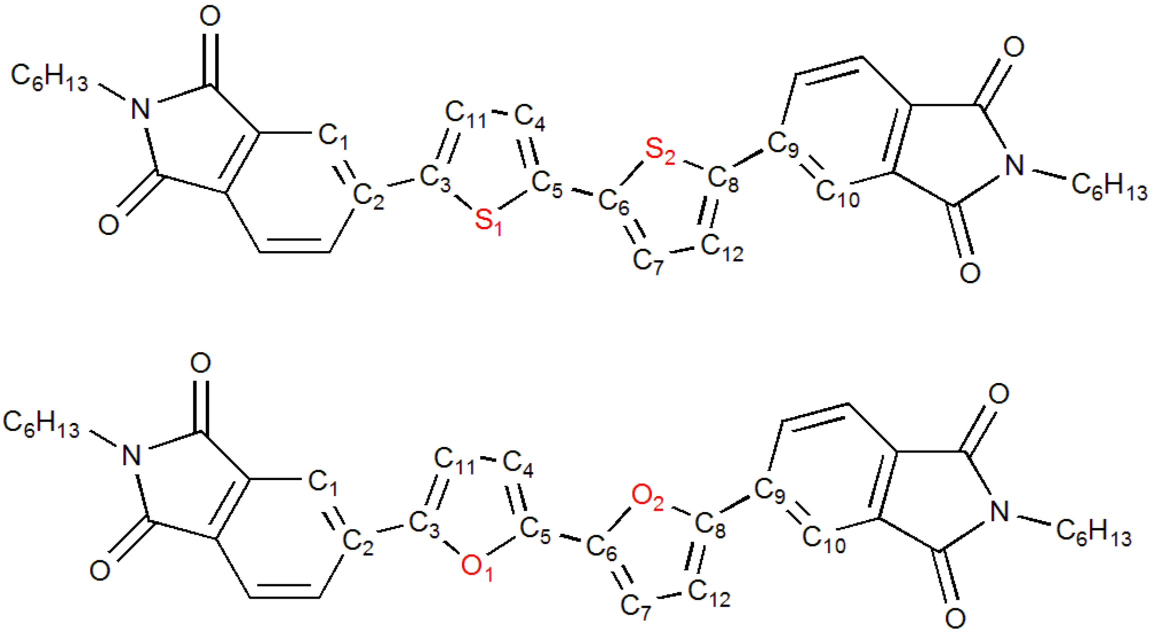

Figure 5.1. Structures of the bi-T (top) and bi-F (bottom)

In this study, geometrical structural changes upon reduction and oxidation, potential energy scans, reorganization energies and transfer integrals have been taken into account to assess the intramolecular and intermolecular charge transfer behavior of the derivatives bi-F and bi-T. The electron and hole mobilities have been calculated to rationalize the difference in electron mobility in these two species.

5.2. Methodology

5.2.1 Reorganization Energies

Charge transport in organic materials may occur in two different ways: hopping-type and band-type [101]. In π-conjugated molecules, hopping-type charge transfer is observed. While an electron is moving from one oligomer to the other, internal arrangements occur on the geometry of the oligomer. Since it controls the charge hopping, this internal reorganization is an important parameter when charge transfer properties of organic materials are in question.

Inner reorganization energy is a result of the alterations in the geometry of a molecule when an electron is removed or added. In order to calculate the reorganization energy, one should know how the conformations and energies of the molecule in the cation and anion states change, and also what the energies of the neutral conformation with an electron added or removed are.

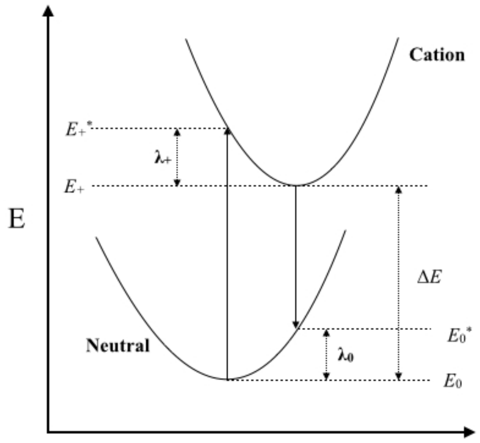

Figure 5.2. Internal reorganization energy $\lambda_+ + \lambda_0$ for hole transfer, and the adiabatic ionization energy, ΔE.

The λ_+ part of the reorganization energy is calculated as the difference of the energy required to go with the neutral conformation to the cation state, and the energy of the cation. The second λ_0 part of the reorganization energy is calculated as the difference of energy required for cation geometry to have neutral state and the energy of the neutral. The sum of the two components gives the hole transfer reorganization energy. Equation 2.65 is a brief summary of this calculation.

$$\lambda = \lambda_0 + \lambda_+ = (E_0^* - E_0) + (E_+^* - E_+) \tag{2.65}$$

For the calculation of electron transfer reorganization, similar calculation is done. The λ_- part of the reorganization energy is calculated as the difference of the energy required to go to the anion state with the neutral conformation, and the energy of the anion state. The second λ_0 part of the reorganization energy is calculated as the difference of energy required for anion geometry to have neutral state and the energy of the neutral state. The sum of the two components gives the electron transfer reorganization energy. Equation

2.66 is a brief summary, and Figure 5.3 is a graphical illustration of this calculation.

$$\lambda = \lambda_0 + \lambda_- = (E_0^* - E_0) + (E_-^* - E_-) \tag{2.66}$$

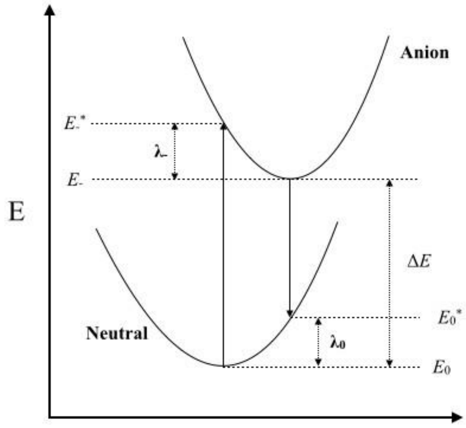

Figure 5.3. Internal reorganization energy $\lambda_- + \lambda_0$ for electron transfer, and the adiabatic ionization energy.

5.2.2. Transfer Integrals

The charge transfer that occurs in a π-conjugated oligomer is influenced greatly by the solid-state packing of the molecules. Intramolecular charge delocalization enhances the charge transfer rates; however molecular structure has an influence on intermolecular charge transfer due to its effects in crystal packing.

Crystal structure information enables computational chemist to calculate charge transfer rates by using Amsterdam Density Functional software package [106]. Transfer integral is a parameter that determines the charge transfer rates. Transfer integral can be explained as the possibility of the transfer of a charge between interacting two molecules.

Transfer integrals are calculated between two monomers of choice, orientation of the molecules can be in various forms such as edge to face, face to face and so on. Determining the overlap of wavefunction of each monomer is an important factor to calculate the charge transfer between two layers.

Simple tight-binding approximation [98],

$$H = \sum_m \epsilon_m a_m^+ a_m + \sum_{m \neq n} t_{mn} a_m^+ a_n \quad (2.67)$$

where a_m^+ and a_m are annihilation and creation operators. ϵ_m is the site energy of the electron at molecular site m and t_{mn} is the charge transfer integral.

The charge carrier mobility in a hopping-type donor material is apporiximated as:

$$k_{ij} = t_{ij}^2 \sqrt{\frac{\pi}{\hbar^2 k_b T \lambda_{ij}}} exp\left(-\frac{(\Delta E_{ij} - \lambda_{ij})^2}{4\lambda_{ij} k_b T}\right) \quad (2.68)$$

where k_{ij} is the Electron Transfer Rate, λ_{ij} is the Reorganization Energy and ΔE_{ij} is the energy difference between the initial and final states.

Orbital energies of a dimer described as:

$$\boldsymbol{HC} - E\boldsymbol{SC} = 0 \quad (2.70)$$

where **H** and **S** are

$$\boldsymbol{H} = \begin{pmatrix} e_1 & J_{12} \\ J_{12} & e_2 \end{pmatrix} \quad (2.71)$$

$$\boldsymbol{S} = \begin{pmatrix} 1 & S_{12} \\ S_{12} & 1 \end{pmatrix} \quad (2.72)$$

And e_i and J_{ij} are

$$e_i = \langle \Psi_i | \widehat{H} | \Psi_i \rangle \quad (2.73)$$

$$J_{ij} = \langle \Psi_i | \widehat{H} | \Psi_j \rangle \quad (2.74)$$

Despite the element e_i and J_{ij} are related to ϵ_i and t_{ij}, they need to be converted into orthonormalized basis. Hereby,

$$H = \begin{pmatrix} e_{12}^{eff} & J_{12}^{eff} \\ J_{12}^{eff} & e_{12}^{eff} \end{pmatrix} \quad (2.75)$$

and $e_{1(2)}^{eff}$ can be calculated as:

$$e_{1(2)}^{eff} = \frac{1}{2}\frac{1(e_1+e_2)-2J_{12}S_{12}\pm(e_1-e_2)\sqrt{1-S_{12}^2}}{1-S_{12}^2} \tag{2.76}$$

$$J_{12}^{eff} = \frac{J_{12}-\frac{1}{2}(e_1+e_2)S_{12}}{1-S_{12}^2} \tag{2.77}$$

Now, e_{12}^{eff} and J_{12}^{eff} are the same as ϵ_i and t_{ij}.

Hence Equation 2.70 becomes

$$\boldsymbol{H}^{eff}\mathbf{C}=\mathrm{E}\mathbf{C} \tag{2.78}$$

The absolute value of the energy difference is then

$$\Delta E_{12} = \sqrt{\left(e_1^{eff} - e_2^{eff}\right)^2 + (2J_{eff}^2)^2} \tag{2.80}$$

5.3. Results

5.3.1. Geometrical Parameters

Bi-F and bi-T have been optimized at various levels by means of the density functional theory since the choice of correct DFT functionals and basis set combination are of uttermost importance. Therefore, benchmark calculations have been applied to the systems of interest. Hybrid functionals such as B3LYP, M06-2X and M06-HF [75] along with the long range corrected hybrid functional ωB97XD have been chosen for benchmark calculations. B3LYP is a well-known density functional for the geometry optimization and ionization energy calculations, alongside M06-2X (%54 HF) and M06-HF (%100 HF) from the Minnesota functionals have been chosen to better understand the effects of increasing Hartree-Fock exchange. Also, because of the long π-conjugation pathway, ωB97XD has been used to take into account these effects. Triple zeta basis set 6-311G** with extra polarization to heavy atoms and hydrogens have been chosen to work with. The chosen functionals have been applied to rubrene and pentacene which have well-known reorganization energies; as a result of the benchmark, the B3LYP/6-311G** methodology has been chosen for this study. The benchmark calculations have been reported in Table 5.1.

Table 5.1. Calculated and experimental hole reorganization energies (meV) of rubrene [107] and pentacene [108].

	Rubrene	**Pentacene**
Experimental	156	100
B3LYP/6-311G**	172	98
ωB97XD/6-311G**	253	171
M06-2X/6-31+G**	225	225
M06-HF/6-311G**	324	292

Table 5.2. summarizes the important geometric parameters of both derivatives in the ground state. Bi-F has kept its planar backbone as reported in the crystal structure [96]. Calculations have revealed the fact that Φ_1 and Φ_3 are slightly larger than the experimental ones by 4.7° and 4.8° respectively. However in bi-T, despite Φ_2 which indicates the planarity of the central part of the molecule, Φ_1 and Φ_3 deviate significantly from the experimental values.

Table 5.2. Selected bond lengths (Å), dihedral angles (Φ in °) of bi-F and bi-T at B3LYP/6-311G** level in $CHCl_3$ (Φ_1 = C1-C2-C3-X1, Φ_2= X1-C5-C6-X2, Φ_3= X2-C8-C9-C10). Experimental values are given in parenthesis [96].

	bi-F	bi-T
C2-C3	1.450 (1.469)	1.463 (1.512)
C3-X1	1.372 (1.388)	1.753 (1.719)
X1-C5	1.365 (1.385)	1.752 (1.720)

Table 5.2. Selected bond lengths (Å), dihedral angles (Φ in °) of bi-F and bi-T at B3LYP/6-311G** level in $CHCl_3$ (Φ_1 = C1-C2-C3-X1, Φ_2= X1-C5-C6-X2, Φ_3= X2-C8-C9-C10). Experimental values are given in parenthesis (cont.) [96].

C5-C6	1.431 (1.438)	1.444 (1.504)
C6-X2	1.365 (1.385)	1.752 (1.720)
X2-C8	1.372 (1.388)	1.753 (1.719)
C8-C9	1.450 (1.469)	1.463 (1.512)
Φ_1	179.55 (174.85)	158.10 (175,92)
Φ_2	180.00 (180)	180 (180)
Φ_3	179.65 (174.85)	158.10 (172.62)

Note that optimization calculations have been carried out for the monomer where the π- π stacking interactions have not been taken into account as opposed to the experimental findings. This may indicate that packing and stacking interactions are significantly more important in bi-T as compared to bi-F, the interaction between layers forces bithiophene to be planar as opposed to bifuran. X-C ((X=O,S) bond lengths and C-C bond distances as well as bond length alternation (BLA) parameters of both compounds have been reported in Table 5.3 and Table 5.4. A low BLA value is a descriptor indicating π-conjugation in a molecule. Both molecules have similar BLA values (0.06) indicating the presence of π-conjugation in both. The X-C bond lengths are coherent with the experimental results, a maximum deviation of 0.2 Å has been observed for the C6-X2 bond in bi-F and 0.34 Å for C3-X1 and X2-C8 bonds in bi-T. The C-C bridges are in agreement with experiment; bi-F has shown a better performance as compared to the bi-T with a deviation of 0.19 Å and 0.49 Å respectively from experiment, the geometrical features of the monomers seem to reproduce the experimental findings even without the contribution of the closest neighbors.

Table 5.3. BLA of Bi-F (Å)

Bi-F	Single Bonds		Double Bonds	BLA
C2-C3	1.450	C3-C11	1.374	
C11-C4	1.418	C4-C5	1.373	
C5-C6	1.431	C6-C7	1.373	
C7-C12	1.418	C8-C12	1.374	
C8-C9	1.450			
Average	1.434		1.373	0.061

Table 5.4. BLA of Bi-T (Å)

Bi-T	Single Bonds		Double Bonds	BLA
C2-C3	1.462	C3-C11	1.377	
C11-C4	1.412	C4-C5	1.379	
C5-C6	1.444	C6-C7	1.379	
C7-C12	1.412	C8-C12	1.377	
C8-C9	1.462			
Average	1.439		1.378	0.061

Table 5.5. Bond length (Å) and dihedral angles (Φ in °) changes of bi-F and bi-T upon oxidation and reduction at B3LYP/6-311G** level in $CHCl_3$ (Φ_1 = C1-C2-C3-C4, Φ_2= X1-C5-C6-X2, Φ_3= C7-C8-C9-C10).

	Oxidation		Reduction	
	bi-F	bi-T	bi-F	bi-T
C2-C3	0.012	0.012	0.018	0.025
C3-X1	0.013	0.010	-0.008	-0.018
X1-C5	0	-0.005	-0.008	-0.016
C5-C6	0.035	0.038	0.016	0.027
C6-X2	0	-0.005	-0.008	-0.016
X2-C8	0.013	0.010	-0.008	-0.018
C8-C9	0.012	0.012	0.018	0.025

Table 5.5. Bond length (Å) and dihedral angles (Φ in °) changes of bi-F and bi-T upon oxidation and reduction at B3LYP/6-311G** level in $CHCl_3$ (Φ_1 = C1-C2-C3-C4, Φ_2= X1-C5-C6-X2, Φ_3= C7-C8-C9-C10). (cont.)

Φ_1	0.35	11.90	0.107	19.82
Φ_2	0	0	0	0
Φ_3	0.35	11.90	0.107	19.82

C-C bridging lengths, C-X bond lengths and dihedral alternations upon the oxidation and reduction processes have been reported in Table 5.5. Dihedral angles of bi-F have hardly changed upon oxidation, Φ_2 remained similar, Φ_1 and Φ_3 have shown deviations by 0.35^0 only, indicating that bi-F has kept its planar backbone and upon oxidation, it is expected that the latter can keep its hole mobility characteristic as well. In contrast to bi-F, dihedral changes of 11.90^0; (Φ_1 and Φ_3) have been observed for bi-T upon oxidation, the latter corresponds to the loss of planarity between the phtalimide moieties and the central ring. Similar findings have been observed for the reduction process as well; the changes for Φ_1 and Φ_3 are even more severe for bi-T in favor of intramolecular electron transfer.

The C5-C6 bond between two thiophene or furan rings alters upon oxidation and reduction. Upon oxidation, both length changes were more significant compared to reduction; it means charge localized on bithiophene and bifuran in oxidation, C5-C6 bond length extended in both derivatives by 0.038 Å and 0.035 Å, respectively. Upon reduction, bi-F and bi-T being planar, charge transfer is supposed to be triggered by the planarity of the backbone.

For bi-F and bi-T potential energy surfaces around Φ_2 have been reported in Fig. 17 and Fig. 18, respectively. bi-F has shown its relative energy minima at 180^0, when backbone of the molecule is planar; in the case of bi-T the minima at 170^0 and there is peak at 200^0; the steric clash in bi-T may be due to the repulsion between the S atoms.

Hereby, the relative energy between eclipsed and staggered conformations of bi-F and bi-T are around 6 kcal/mol and 3 kcal/mol, respectively.

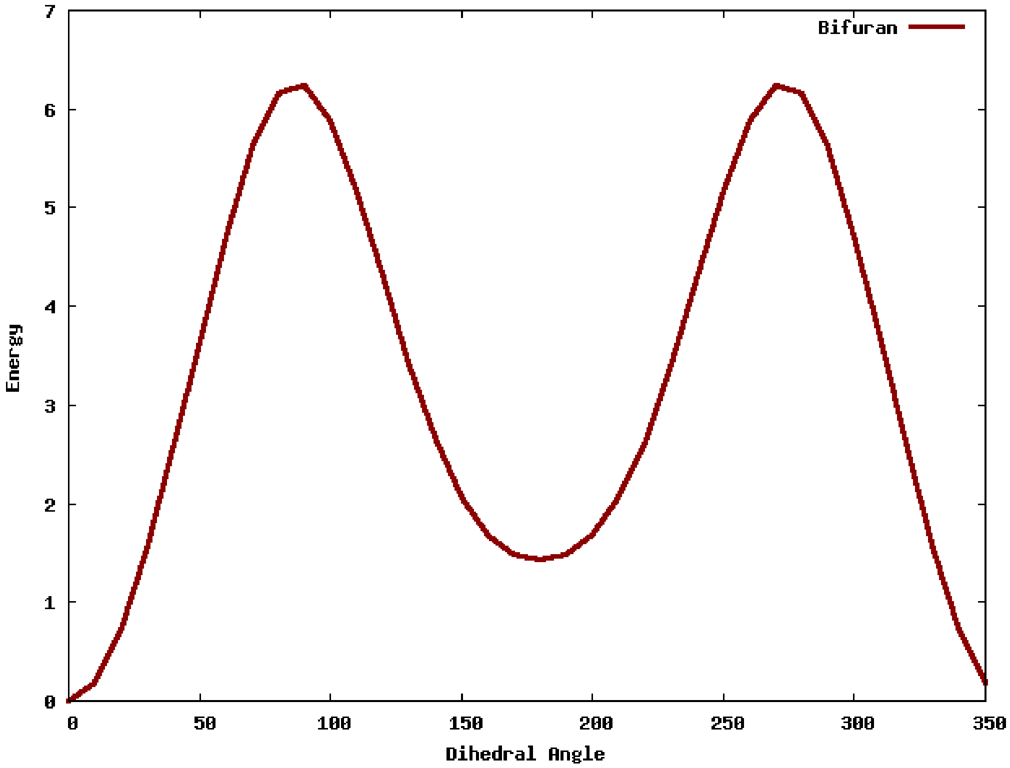

Fig 5.4. Potential Energy Surface (kcal/mol) of bi-F

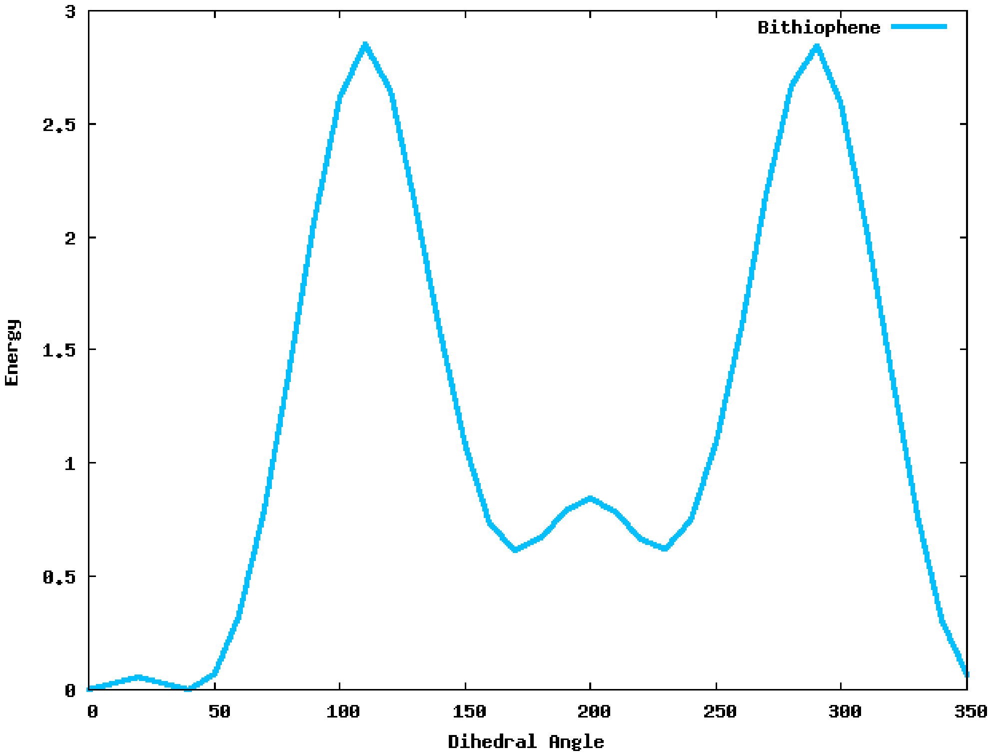

Fig 5.5. Potential Energy Surface (kcal/mol) of bi-T

5.3.2. Reorganization Energies

π-conjugated molecules show thermally activated hopping-type charge transfer characteristics at high temperatures [109]. Reorganization energy is an important parameter along with electronic coupling between adjacent molecules, to better analyze the charge transfer phenomena, also it provides important information to analyze the geometry relaxations that occur in a system during charge alternation and provides an important evaluation of electron-phonon coupling. High reorganization energies can be interpreted as low mobility. Ionization energies (IP) and electron affinities (EA) can be used to demonstrate how easily charge replacement can occur within the molecules; a low VIP indicates an easy oxidation based on removal of an electron, whereas a high VEA indicates easy reduction based on electron addition.

Table 5.6. Calculated (B3LYP/6-311G**) Reorganization Energies (meV), VIP, AIP, VEA and AEA (eV) in $CHCl_3$. Experimental values are given in parenthesis.

	λ_{hole}	$\lambda_{electron}$	VIP	AIP	VEA	AEA
bi-F	234.32	234.12	5.8 (5.68)	5.68	-2.63 (2.98)	-2.74
bi-T	170.32	233.90	6.09 (5.52)	6.00	-2.62 (-3.05)	-2.76

VIP, AIP, VEA and AEA are displayed in Table 5.6. Experimental VIP and VEA values have been compared with the computed values to rationalize the accuracy of the findings. Indeed, one can see that differences with experiment are less than 0.6 eV. Furthermore, bi-F has only shown 0.12 eV and 0.35 eV deviations from the experimental results for VIP and VEA, respectively. For bi-T, deviations from the experiment are higher, 0.57 eV for VIP and 0.43 eV for VEA.

Computed hole reorganization energy (λ_{Hole}) and electron reorganization energy ($\lambda_{Electron}$) of the bi-F are fairly similar with the values of 234.32 meV and 234.12 meV, respectively. Internal reorganization energies depend on the charge delocalization. The former quantities indicate that upon oxidation and reduction processes in bi-F, charge carriers are similarly localized. Thereof, intramolecular charge transfer between the continuous layers can be the main reason of the unusual mobility loss of the bi-F. Furthermore, $\lambda_{electron}$ of bi-T with value of 233.90 is almost similar to the bi-F, which demonstrates that upon the reduction process both molecules are going under equal amount of geometry alternation. Also the similar charge transfer behavior from the central rings to the side moieties is observed in the monomers of both derivatives. This can be the reason of such close reorganization energies. On the other hand, λ_{hole} of the thiophene derivative conspicuously smaller compared to the other computed reorganization energies. Overall, calculated reorganization energies indicate that, intramolecular geometry relaxations of both derivatives are fairly similar and unlikely to be the reason of electron mobility loss of the bi-F.

5.3.3. Charge Transfer Integrals of the Crystals.

Packing in the solid state is influenced mainly by the chemical structures of the π-conjugated molecules. Charge transfer integrals between adjacent molecules can be calculated from experimentally known crystal structures. Furthermore, transfer integrals can be reliable indeces to compare charge transfer rates of the molecules. Transfer integrals can be used to understand the contribution of different dimers to the aggregated entity. In this section, the experimentally known crystal structures of both derivatives have been used to assess the charge transfer integrals between dimers [96]. The solid-state packing of the derivatives are displayed in Figure 5.6. One may see that, despite the substitution of sulfur atom to oxygen on the central rings, both derivatives have similar packing in the solid state. Also, note that the side chains have an important role in the charge transfer between adjacent molecules.

The calculated transfer integrals of holes (t_{hole}) and electrons ($t_{electron}$) of derivatives and the centroid to centroid distance between adjacent molecules are reported in Table 5.7. All plausible dimers for the hole/electron transfer have been taken into the account. Among all, dimer 12 has shown the highest charge transfer integrals for both derivatives with t_{hole} values of 65.4, 75.2 and $t_{electron}$ values of -0.07, 22.4 for bi-F and bi-T, respectively; as expected, due to its close centroid to centroid distance. Note that besides the distance between centroids, the orientation of the molecules plays a role in the charge transfer integrals. For instance, dimer 13 has a smaller charge transfer integral compared to dimer 14 despite the shorter centroid to centroid distance. t_{hole} of bi-T and bi-F have been calculated in dimer 12 with values of -75 meV and -65 meV, respectively. However, while bi-T has 22 meV for the $t_{electron}$, bi-F has shown almost no charge transfer at all. This indicates that intramolecular charge transfer does not occur in bi-F unlike the bi-T, despite the same face to face π-stacking with similar centroid to centroid distances between adjacent layers of 5.021 Å and 5.002 Å, respectively.

Figure 5.6. Solid state packing of the molecules

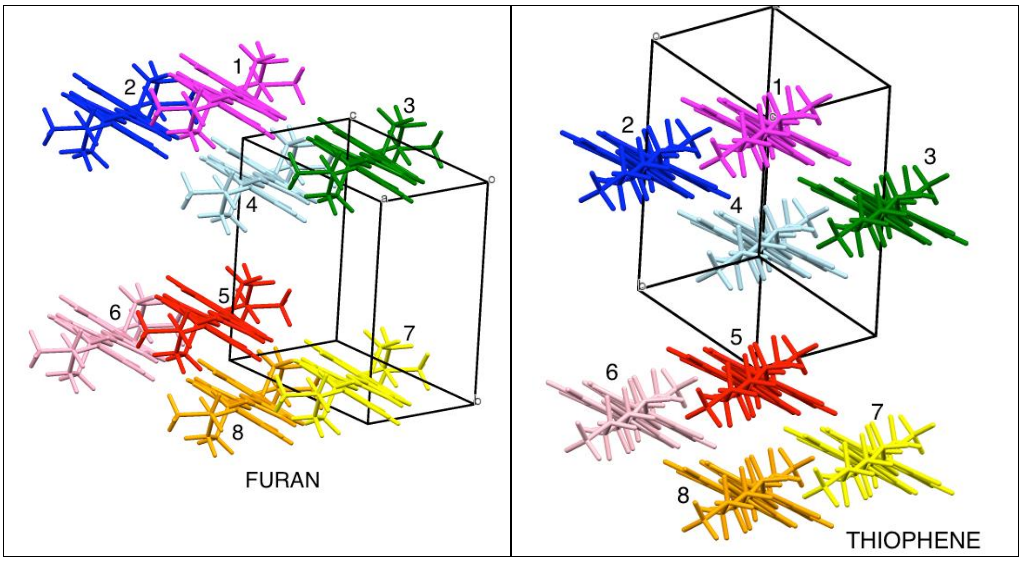

Table 5.7. Calculated Transfer Integrals (meV), centroid to centroid distances (Å) of Bi-F and Bi-T

	Bi-F			**Bi-T**		
DIMER	t_{hole}	$t_{electron}$	**d**	t_{hole}	$t_{electron}$	**d**
12	-65.40	-0.07	5.002	-75.15	22.44	5.021
13	0.16	4.07	14.482	0.33	4.86	14.579
14	-5.55	7.45	16.015	-7.57	5.44	15.071
15	-0.02	0.01	11.552	0.03	0.03	11.022
16	0	0	12.22	0	0	11.644
23	0	-0.01	14.595	0	-0.13	15.76
24	0.16	4.07	14.482	0.33	4.86	14.579
25	-0.03	0.42	12.893	-0.13	1.11	12.562
26	-0.02	0.01	11.552	0.03	0.03	11.022
34	-65.40	-0.07	5.002	-75.15	22.44	5.021

Table 5.7. Calculated Transfer Integrals (meV), centroid to centroid distances (Å) of Bi-F and Bi-T (cont.)

35	0.01	-0.02	21.045	-0.01	0.01	20.76
36	0	0	20.922	0	0	21.347
45	-2.57	0.35	22.318	-0.11	-0.05	21.369
46	0.01	-0.02	21.045	-0.01	0.01	20.76

5.4. Conclusion and Future Work

Bi-T and bi-F monomers are modeled and their various intramolecular and intermolecular properties have been investigated computationally. A benchmark test, based on the use of hybrid and long range corrected density functionals has been performed to understand the importance of non-local exchange and long range correction to optimization of the molecules and calculation of the reorganization energies. The results of the benchmark indicate that hybrid B3LYP, along with 6-311G** basis set performed the best to calculate reorganization energies.

Investigations of the geometrical parameters have shown that reproduction of the experimental results was accomplished, even without the contribution of adjacent layers. However, one should note that the solid state packing interactions, thus the interactions between adjacent layers are more important in bi-T compared to bi-F to maintain the planar backbone. Also, bond length alternation results of the monomers demonstrate the similar presence of the π-conjugation in both derivatives.

The hole reorganization energies have shown that, while hole reorganization energies of the both derivatives are different with values of 234.32 meV for bi-F and 170.32 for bi-T, electron reorganization energies were similar. Accordingly, intramolecular geometry relaxations of both derivatives were similar and unlikely to be reason of electron mobility loss of the bi-F. Transfer integral calculations have shown that, intermolecular charge transfer is the main cause of electron mobility loss in bi-F. Especially, in the Dimer 12 which has the closest centroid to centroid distance in the crystal packing, bi-F has not shown any charge transfer.

As a future work, theoretical mobility of the derivatives will be calculated by applying Marcus Theory. Also, molecular dynamic calculations will be held to further analyze the intermolecular charge transfer behaviors and their structure-property relationships.

REFERENCES

1. Whitesides, G. M., Simanek, E. E., Mathias, J. P., Seto, C. T., Chin, D., Mammen, M., Gordon, D. M., “Noncovalent Synthesis: Using Physical-Organic Chemistry To Make Aggregates What Kinds of Structures Should Organic Chemists Be Learning To Make?”, *Accounts of Chemical Research,* Vol. 28, No. 1, pp. 37-44, 1995.

2. Bostan, A., Gheorge, A. V, Dulgheru, V., "*Resilient Energy Systems : Renewables: Wind, Solar, Hydro*", Springer Dordrecht Heidelber New York London, 2013.

3. Kamat, P. V., “Meeting the Clean Energy Demand: Nanostructure Architectures for Solar Energy Conversion", *The Journal of Physical Chemistry C*, Vol. 111, No. 7, pp. 2834-2860, 2007.

4. Hagfeldt, A., Boschloo, G., Sun, L. Kloo, L., and Pettersson, H., “Dye-Sensitized Solar Cells”, *Chemical. Reviews*, Vol. 110, No. 11, pp. 6595–6663, 2010.

5. Grätzel, M., “Recent Advances in Sensitized Mesoscopic Solar Cells”, *Accounts of Chemical Research*, Vol. 42, no. 11, pp. 1788–1798, 2009.

6. Jun, H. K., Careem, M. A., Arof, A. K., “A Suitable Polysulfide Electrolyte for CdSe Quantum Dot-Sensitized Solar Cells”, *International Journal of Photoenergy*, Vol. 2013, pp. 1–10, 2013.

7. O’Regan, B., Grätzel, M., “A low-cost, high-efficiency solar cell based on dye-sensitized colloidal TiO2 films”, *Nature*, Vol. 353, No. 6346, pp. 737–740, 1991.

8. Kojima, A., Teshima, K., Shirai, Y., Miyasaka, T., “Organometal Halide Perovskites as Visible-Light Sensitizers for Photovoltaic Cells”, *Journal of the American Chemical Society*, Vol. 131, No. 17, pp. 6050–6051, 2009.

9. Dennler, G., Scharber, M. C., Brabec, C. J., “Polymer-Fullerene Bulk-Heterojunction Solar Cells”, *Advanced Materials*, Vol. 21, No. 13, pp. 1323–1338, 2009.

10. Brabec, C. J. *et al.*, "Polymer-Fullerene Bulk-Heterojunction Solar Cells”, *Advanced Materials*, Vol. 22, No. 34, pp. 3839–3856, 2010.

11. Tang, C. W., “Two-layer organic photovoltaic cell”, *Applied Physics Letters*, vol. 48, no. 2, p. 183, 1986.

12. Karg, S., Riess, W., Dyakonov, V., Schwoerer, M., “Electrical and optical characterization of poly(phenylene-vinylene) light emitting diodes”, *Synthetic Metals*, Vol. 54, No. 1, pp. 427–433, 1993.

13. Cheng, Y. J., Yang, S. H., and Hsu, C. S., “Synthesis of Conjugated Polymers for Organic Solar Cell Applications”, *Chemical Reviews*, Vol. 109, No. 11, pp. 5868–5923, 2009.

14. Mishra, A., Bauerle, P., “Small Molecule Organic Semiconductors on the Move: Promises for Future Solar Energy Technology”, *Angewandte Chemie International Edition*, Vol. 51, No. 9, pp. 2020–2067, 2012.

15. Kippelen, B., Bredas J. C, Becquerel, E., Chapin, D. M., “Organic photovoltaics", *Energy & Environmental Science*, Vol. 2, No. 3, pp. 251-261, 2009.

16. Scharber, M. C., Mühlbacher, D., Koppe, M., Denk, P., Waldauf, C., Heeger, A. J., Brabec, C. J., “Design Rules for Donors in Bulk-Heterojunction Solar Cells—Towards 10 % Energy-Conversion Efficiency”, *Advanced Materials*, Vol. 18, No. 6, pp. 789–794, 2006.

17. Brabec, C. J., Sarıçiftçi, N. S., Hummelen, J. C., “Plastic Solar Cells”, *Advanced Functional Materials*, Vol. 11, No. 1, pp. 15–26, 2001.

18. Güneş, S., Neugebauer, H., Sarıçiftçi, N. S., “Conjugated Polymer-Based Organic Solar Cells”, *Chemical Reviews*, Vol. 107, pp. 1324-1338, 2007.

19. Wudl, F., “The chemical properties of buckminsterfullerene (C60) and the birth and infancy of fulleroids”, *Accounts of Chemical Research*, Vol. 25, No. 3, pp. 157–161,

1992.

20. Fitzner, R., Reinold, E., Mishra, A., Osteritz, E., Ziehlke, H., Körner, C., Leo, K., Riede, M., Weil, M., Tsaryova, O., Weiß, A., Uhrich, C., Pfeiffer, M., and Bäuerle, P., "Dicyanovinyl-Substituted Oligothiophenes: Structure-Property Relationships and Application in Vacuum-Processed Small Molecule Organic Solar Cells", *Advanced Functional Materials,* Vol. 21, No. 5, pp. 897–910, 2011.

21. Haid, S., Mishra, A. Weil, M., Uhrich, C., Pfeiffer, M., and Bäuerle, P., "Synthesis and Structure-Property Correlations of Dicyanovinyl-Substituted Oligoselenophenes and their Application in Organic Solar Cells", *Advanced Functional Materials*, Vol. 22, No. 20, pp. 4322–4333, 2012.

22. Walker, B., Tamayo, A. B., Dang, X.-D., Zalar, P., Seo, J. H., Garcia, A., Tantiwiwat, M., Nguyen, T.-Q., "Nanoscale Phase Separation and High Photovoltaic Efficiency in Solution-Processed, Small-Molecule Bulk Heterojunction Solar Cells", *Advanced Functional Materials,* Vol. 19, No. 19, pp. 3063–3069, 2009.

23. Parr, R. G., Weitao, T., "*Density Functional Theory of Atoms and Molecules*", Oxford University Press, 1989.

24. Becke, A. D., "A New Mixing of Hartree–Fock and Local Density Functional Theories", *The Journal of Chemical Physics,* Vol. 98, No. 2, pp. 1372-1377, 1993.

25. Becke, A. D., "Density Functional Exchange Energy Approximation with Correct Asymptotic Behavior", *Physical Review A,* Vol. 38, No. 6, pp. 3098–3100, 1988.

26. Roos, B. O., "*Lecture Notes in Quantum Chemistry II"*, vol. 64. Springer Berlin Heidelberg, 1994.

27. Leach, A. R., "*Molecular Modelling. Principles and Applications (2nd Edition) by Andrew R. Leach*", Prentice Hall, 2001.

28. Lee, C., Weitao, Y., Parr, G. R., "Development of the Colle-Salvetti Correlation

Energy Formula into a Functional of the Electron Density”, *Physical Review B,* Vol. 37, No. 2, pp. 785–789, 1988.

29. Becke, A. D., “Density Functional Thermochemistry. III. The role of exact exchange”, *The Journal of Chemical Physics,* Vol. 98, pp. 5648-5652, 1993.

30. Pauling, L., “The Nature of the Chemical Bond. IV. The Energy of Single Bonds and the Relavitve Electronegativity of Atoms”, *Journal of the American Chemical Society,* Vol. 54, No. 9, pp. 3570–3582, 1932.

31. Tapia, B. J., "*Solvent Effects and Chemical Reactivity*", Kluwer Academic Publishers, 1984.

32. Cramer, J. C., Truhlar, D. G., “Implicit Solvation Models: Equilibria, Structure, Spectra, and Dynamics”, *Chemical Reviews,* Vol. 99, No. 8, pp. 2161-2200, 1999.

33. Tomasi, J., Mennucci, B., Cammi, R., “Quantum Mechanical Continuum Solvation Models”, *Chemical Reviews,* Vol. 105, No. 8, pp. 2999-3094, 2005.

34. Barone, V., Cossi, M., Tomasi, J., "Geometry optimization of molecular structures in solution by the polarizable continuum model”, *Journal of Computational Chemistry,* Vol. 19, No. 4, pp. 404–417, 1998.

35. Barone, V., Cossi, M., “Quantum Calculation of Molecular Energies and Energy Gradients in Solution by a Conductor Solvent Model”, *The Journal of Physical Chemistry A,* Vol. 102, No. 11, pp. 1995-2001, 1998.

36. Liao, J., Zhao, H., Xu, Y., Cai, Z., "Novel D–A–D type dyes based on BODIPY platform for solution processed organic solar cells”, *Dyes and Pigments,* Vol. 128, pp. 131–140, 2016.

37. Ke, J. C., Wang, Y., Chen, K., Huang, C., “Effect of organic solar cells using various sheet resistances of indium tin oxide and different cathodes: Aluminum, silver”, *Synthetic Metals,* Vol. 201, pp. 25–29, 2015.

38. Entwistle, C. D., Collings, J. C., Steffen A., Palsson, L. O., Beeby, A., Jove, D., Burke, J. M., Batsanov, A. S., Howard, J. A. K., Mosely, J. A., Poon, S. Y., Wang, W. Y., Ibersiene, F., Fathallah, S., Boucekkine, A., Halet, J. F., Marder, T. B., “Syntheses, structures, two-photon absorption cross-sections and computed second hyperpolarisabilities of quadrupolar A–π–A systems containing E-dimesitylborylethenyl acceptors”, *Journal of Materials Chemistry*, Vol. 19, No. 40, pp. 7532-7544, 2009.

39. Hoffend, C., Diefenbach, M., Januszewksi, E., “Effects of boron doping on the structural and optoelectronic properties of 9,10-diarylanthracenes”, *Dalton Transactions*, Vol. 42, No. 38, pp. 13826-13837, 2013.

40. Parab, K., Venkatasubbaiah K., Jakle, F., “Luminescent Triarylborane-Functionalized Polystyrene: Synthesis, Photophysical Characterization, and Anion-Binding Studies”, *Journal of the American Chemical Society,* Vol. 128, No. 39, pp. 12879–12885, 2006.

41. Chu, C., Tu, Y., Hasiao, J., “Combination of photothermal and photodynamic inactivation of cancer cells through surface plasmon resonance of a gold nanoring”, *Nanotechnology,* Vol. 27, No. 11, pp. 102-115, 2016.

42. Masters, B. R., So. P., “Antecedents of two-photon excitation laser scanning microscopy”, *Microscopy Research and Technique,* Vol. 63, No. 1, pp. 3–11, 2004.

43. Lee, K. S., "*Polymers for Photonics Applications II*", vol. 161. Springer Berlin .Heidelberg, 2003.

44. Pawlicki, M., Collins H., Denning, R. G., Anderson, H. L., “Two-photon absorption and the design of two-photon dyes”, *Angewandte Chemie (International ed. in English),* Vol. 48, No. 18, pp. 3244–3266, 2009.

45. Tkachenko, N., “Optical Spectroscopy", Elsevier, 2016

46 Karatay, A., Miser, X., Cui, X., “The effect of heavy atom to two photon absorption properties and intersystem crossing mechanism in aza-boron-dipyrromethene compounds”, *Dyes and Pigments*, Vol. 122, pp. 286–294, 2015.

47. Gierschner, J., Cornil, J., Egelhaaf, H., “Optical Bandgaps of π-Conjugated Organic Materials at the Polymer Limit: Experiment and Theory”, *Advanced Materials*, Vol. 19, No. 2, pp. 173–191, 2007.

48. Pandey, L., Doiron, C., Sears, J., Bredas, J. L., “Lowest excited states and optical absorption spectra of donor-acceptor copolymers for organic photovoltaics: a new picture emerging from tuned long-range corrected density functionals”, *Physical Chemistry Chemical Physics,* Vol. 14, No. 41, pp. 14243–14248, 2012.

49. Pastore, M., “Benzylic Amide Rotaxanes: A Versatile Architecture”, *Current Organic Synthesis*, Vol. 9, No. 2, pp. 215–232, 2012.

50. Salvatori, P., Mosconi, E., Wang, E., “Computational Modeling of Isoindigo-Based Polymers Used in Organic Solar Cells”, *The Journal of Physical Chemistry C*, Vol. 117, No. 35, pp. 17940–17954, 2013.

51. Erbay, T. G., Aviyente, V., Salman, S., “How substitution tunes the electronic and transport properties of oligothiophenes, oligoselenophenes and oligotellurophenes”, *Synthetic Metals,* Vol. 210, pp. 236–244, 2015.

52. Pandey, L., Risko, C., Norton, J., Bredas, J. L., “Donor–Acceptor Copolymers of Relevance for Organic Photovoltaics: A Theoretical Investigation of the Impact of Chemical Structure Modifications on the Electronic and Optical Properties”, *Macromolecules*, Vol. 45, No. 16, pp. 6405–6414, 2012.

53. D’Avino, G., Muccioli, L., Olivier, Y., Beljonne, D., “Charge Separation and Recombination at Polymer-Fullerene Heterojunctions: Delocalization and Hybridization Effects”, *The Journal of Physical Chemistry Letters*, Vol. 7, No. 3, pp. 536–40, 2016.

54. Avilov, I., Geskin, V., Cornil, J., “Quantum-Chemical Characterization of the Origin of Dipole Formation at Molecular Organic/Organic Interfaces”, *Advanced Functional Materials*, Vol. 19, No. 4, pp. 624–633, 2009.

55. Pastore, M., De Angelis, F., “Modeling materials and processes in dye-sensitized solar cells: understanding the mechanism, improving the efficiency”, *Topics in Current*

Chemistry, Vol. 352, pp. 151–236, 2014.

56 Kanai, Y., Grossman, J. C., “Insights on interfacial charge transfer across P3HT/fullerene photovoltaic heterojunction from Ab initio calculations.,” *Nano Letters*, Vol. 7, No. 7, pp. 1967–72, 2007.

57. Kim, B. G., Ma. X., Chen, C., “Energy Level Modulation of HOMO, LUMO, and Band-Gap in Conjugated Polymers for Organic Photovoltaic Applications” *Advanced Functional Materials,* Vol. 23, No. 4, pp. 439–445, 2013.

58. Ip, C. M., Eleuteri, A., Troisi, A., “Predicting with confidence the efficiency of new dyes in dye sensitized solar cells” *Physical Chemistry Chemical Physics*, Vol. 16, No. 36, pp. 19106-19110, 2014.

59 Tortorella, S., Talamo, M., Cardone, A., Pastore, M., De Angelis, F., “Benchmarking .DFT and semi-empirical methods for a reliable and cost-efficient computational screening of benzofulvene derivatives as donor materials for small-molecule organic solar cells” *Journal of Physics Condensed Matter,* Vol. 28, No. 7, p. 74005, 2016.

60. Akimov, A. V., Prezhdo, O. V., “Large-Scale Computations in Chemistry: A Bird’s Eye View of a Vibrant Field” *Chemical Reviews*, Vol. 115, No. 12, pp. 5797–890, 2015.

61. Dreuw, A., Head-Gordon, M., “Failure of time-dependent density functional theory for long-range charge-transfer excited states: the zincbacteriochlorin-bacteriochlorin and bacteriochlorophyll-spheroidene complexes.,” *Journal of the American Chemical Society,* Vol. 126, No. 12, pp. 4007–4016, 2004.

62. A. Dreuw, J. *et al.*, “Long-range charge-transfer excited states in time-dependent density functional theory require non-local exchange” *Journal of Chemical Physics*, Vol. 119, No. 6, pp. 2943-2946, 2003.

63. Liu X., Subotnik, J. E., “The Variationally Orbital-Adapted Configuration Interaction Singles (VOA-CIS) Approach to Electronically Excited States” *Journal of Computational Chemistry,* Vol. 10, No. 3, pp. 1004–1020, 2014.

64. Huang, S. *et al.*, “Computational Prediction for Singlet- and Triplet-Transition Energies of Charge-Transfer Compounds” *Journal of Chemical Theory and Computation*, Vol. 9, No. 9, pp. 3872–3877, 2013.

65. Yanai, T. *et al.*, “A new hybrid exchange–correlation functional using the Coulomb-attenuating method (CAM-B3LYP)” *Chemical Physics Letters,* Vol. 393, No. 1–3, pp. 51–57, 2004.
66. Baer R., Neuhauser, D., “Density functional theory with correct long-range asymptotic behavior” *Physical Review Letters*, Vol. 94, No. 4, pp. 43002, 2005.

67. Chai, J.-D., Head-Gordon, M., “Long-range corrected hybrid density functionals with damped atom-atom dispersion corrections” *Physical Chemistry Chemical Physics*, Vol. 10, No. 44, pp. 6615–6620, 2008.

68. Vydrov, O. A., Scuseria, G. E., “Assessment of a long-range corrected hybrid functional” *The Journal of Chemical Physics*, Vol. 125, No. 23, pp. 234109-234118, 2006.

69. Karton, A. *et al.*, “Highly Accurate First-Principles Benchmark Data Sets for the Parametrization and Validation of Density Functional and Other Approximate Methods. Derivation of a Robust, Generally Applicable, Double-Hybrid Functional for Thermochemistry and Thermochemical” *The Journal of Physical Chemistry A*, Vol. 112, No. 50, pp. 12868–12886, 2008.

70 Goerigk, L., Moellmann, J., Grimme, S., “Computation of accurate excitation energies for large organic molecules with double-hybrid density functionals” *Physical Chemistry Chemical Physics*, vol. 11, no. 22, p. 4611, May 2009.

71. Wigner, E., “On the Quantum Correction For Thermodynamic Equilibrium” *Physical Review,* Vol. 40, No. 5, pp. 749–759, 1932.

72. Etienne, T., Assfeld, X., Monari, A., “Toward a Quantitative Assessment of Electronic Transitions’ Charge-Transfer Character” *Journal of Chemical Theory and Computation,* Vol. 10, No. 9, pp. 3896–905, 2014.

73. Etienne, T., Assfeld, X., Monari, A., “New Insight into the Topology of Excited States through Detachment/Attachment Density Matrices-Based Centroids of Charge” *Journal of Chemical Theory and Computation*, Vol. 10, No. 9, pp. 3906–14, 2014.

74. Slater, J. C., “A Simplification of the Hartree-Fock Method,” *Physical Review,* Vol. 81, No. 3, pp. 385–390, 1951.

75. Zhao, Y., Truhlar, D. G., “The M06 suite of density functionals for main group thermochemistry, thermochemical kinetics, noncovalent interactions, excited states, and transition elements: two new functionals and systematic testing of four M06-class functionals and 12 other function” *Theoretical Chemistry Accounts*, Vol. 120, No. 1–3, pp. 215–241, 2007.

76. Becke, A. D., “Density-functional thermochemistry. III. The role of exact exchange” *Journal of Chemical Physics*, Vol. 98, No. 7, p. 5648, 1993.

77. Lee C., Yang, W., Parr, R. G., “Development of the Colle-Salvetti correlation-energy formula into a functional of the electron density” *Physical Review B*, Vol. 37, No. 2, pp. 785–789, 1988.

78. Lynch, B. J., Fast, P. L., Harris, M., Truhlar, D. G., “Adiabatic Connection for Kinetics” *The Journal of Physical Chemistry A*, Vol. 104, No. 21, pp. 4811–4815, 2000.

79. Chai, J. D., Head-Gordon, M., “Long-range corrected hybrid density functionals with damped atom-atom dispersion corrections” *Physical Chemistry Chemical Physics*, Vol. 10, No. 44, pp. 6615–6620, 2008.

80. Zhao, Y., Lynch, B. J., Truhlar, D. G., “Doubly Hybrid Meta DFT: New Multi-Coefficient Correlation and Density Functional Methods for Thermochemistry and Thermochemical Kinetics” *The Journal of Physical Chemistry A*, Vol. 108, No. 21, pp. 4786–4791, 2004.

81. Schwabe, T., Grimme, S., “Towards chemical accuracy for the thermodynamics of

large molecules: new hybrid density functionals including non-local correlation effects” *Physical Chemistry Chemical Physics*, Vol. 8, No. 38, pp. 4398–401, 2006.

82. Schwabe, T., Grimme, S., “Double-hybrid density functionals with long-range dispersion corrections: higher accuracy and extended applicability” *Physical Chemistry Chemical Physics*, Vol. 9, No. 26, pp. 3397–406, 2007.

83. Tomasi, J., Mennucci, B., Cammi, R., “Quantum mechanical continuum solvation models” *Chemical Reviews*, Vol. 105, No. 8, pp. 2999–3093, 2005.

84. Pastore, M., Mosconi, E., Angelis, F., Grätzel, M., “A Computational Investigation of Organic Dyes for Dye-Sensitized Solar Cells: Benchmark, Strategies, and Open Issues” *The Journal of Physical Chemistry C*, Vol. 114, No. 15, pp. 7205–7212, 2010.

85. Neese, F., “The ORCA program system” *Wiley Interdisciplinary Reviews: Computational Molecular Science*, Vol. 2, No. 1, pp. 73–78, 2012.

86. Di Meo, F., Trouillas, P., Adamo, C., Sancho-García, J. C., “Application of recent double-hybrid density functionals to low-lying singlet-singlet excitation energies of large organic compounds” *Journal of Chemical Physics*, Vol. 139, No. 16, p. 164104, 2013.

87. Neese, F., Wennmohs, F., Hansen, A., Becker, U., “Efficient, approximate and parallel Hartree–Fock and hybrid DFT calculations. A ‘chain-of-spheres’ algorithm for the Hartree–Fock exchange” *Chemical Physics*, Vol. 356, No. 1–3, pp. 98–109, 2009.

88. Neese, F., “An improvement of the resolution of the identity approximation for the formation of the Coulomb matrix” *Journal of Computational Chemistry*, Vol. 24, No. 14, pp. 1740–1747, 2003.

89. Etienne, T., “Probing the Locality of Excited States with Linear Algebra” *Journal of Chemical Theory and Computation*, Vol. 11, No. 4, pp. 1692–1699, 2015.

90. Dahl, J. P., Springborg, M., “The Morse oscillator in position space, momentum space, and phase space” *Journal of Chemical Physics*, Vol. 88, No. 7, p. 4535, 1988.

91. Schinke, R., “Photodissociation Dynamics: Spectroscopy and Fragmentation of Small Polyatomic Molecules" Cambridge University Press, 2006

92. Barbatti, M., Ruckenbauer, M., Plasser, F., Pittner, J., Granucci, G., Persico, M., Lischka, H., “Newton-X: a surface-hopping program for nonadiabatic molecular dynamics” *Wiley Interdisciplinary Reviews: Computational Molecular Science*, Vol. 4, No. 1, pp. 26–33, 2014.

93. Lin, N., Luo, Y., Ruud, K., Zhao, X., Santoro, F., Rizzo, A., “Differences in two-photon and one-photon absorption profiles induced by vibronic coupling: the case of dioxaborine heterocyclic dye” *ChemPhysChem*, Vol. 12, No. 17, pp. 3392–403, 2011.

94. “Dalton,” 2015. [Online]. http://www.daltonprogram.org/, accessed at December 2016

95. Turan, H. T., Eken, Y., Marazzi, M., Pastore, M., Aviyente, V., Monari, A., “Assessing One-and Two-Photon Optical Properties of Boron Containing Arenes” *The Journal of Physical Chemistry C,* Vol. 120, pp. 17916-7926, 2016

96 Hendsbee, A. D., Sun, J. P., McCormick, T. M., Hill, I. G., Welch, G. C., “Unusual loss of electron mobility upon furan for thiophene substitution in a molecular semiconductor,” *Organic Electronics*, Vol. 18, pp. 118–125, 2015.

97. Liu, J., Walker, B., Tamayo, A., Zhang, Y., Nguyen, T. Q., “Effects of Heteroatom Substitutions on the Crystal Structure, Film Formation, and Optoelectronic Properties of Diketopyrrolopyrrole-Based Materials” *Advanced Functional Materials,* Vol. 23, No. 1, pp. 47–56, 2013.

98. Valeev, F., Coropceanu, V., Filho, D. A., Salman, S, Brédas J. L., “Effect of Electronic Polarization on Charge-Transport Parameters in Molecular Organic Semiconductors” *Journal of the American Chemical Society,* Vol. 128, No. 30, pp. 9882-9886, 2006.

99 Lan, Y.-K., Huang, C.-I., “A Theoretical Study of the Charge Transfer Behavior of the Highly Regioregular Poly-3-hexylthiophene in the Ordered State” *The Journal of Physical Chemistry B*, Vol. 112, No. 47, pp. 14857–14862, 2008.

100. Schweicher, G., Olivier, Y., Lemaur, V., Geerts, Y. H., “What Currently Limits Charge Carrier Mobility in Crystals of Molecular Semiconductors?” *Israel Journal of Chemistry*, Vol. 54, No. 5–6, pp. 595–620, 2014.

101. Coropceanu, V., Cornil, J., Filho, D. A., Olivier, Y., Silbey, R., Brédas J L., “Charge Transport in Organic Semiconductors” *Chemical Reviews*, Vol. 107, No. 4, pp. 926-952, 2007.

102. Nelson, J., Kwiatkowski, J. J., Kirkpatrick, J., Frost, J. M., “Modeling Charge Transport in Organic Photovoltaic Materials” *Accounts of Chemical Research*, Vol. 42, No. 11, pp. 1768–1778, 2009.

103. Zhao, Y., Liang, W., Peumans, P., Yakimov A., “Charge transfer in organic molecules for solar cells: theoretical perspective” *Chemical Society Reviews*, Vol. 41, No. 3, pp. 1075–1087, 2012.

104. Baumeier, B., May, F., Lennartz, C., Andrienko, D., “Challenges for in silico design of organic semiconductors” *Journal of Materials Chemistry* Vol. 22, No. 22, pp. 10971-10976, 2012.

105. Kyono, A., Hayakawa, A., Horiki, M., “Selenium substitution effect on crystal structure of stibnite (Sb2S3)” *Physics and Chemistry of Minerals*, Vol. 42, No. 6, pp. 475–490, 2015.

106. Guerra, C. F., Snijders, J. G, Velde G., Baerends, E. J., “Towards an order- N DFT method” *Theoretical Chemistry Accounts: Theory, Computation, and Modeling*, Vol. 99, No. 6, pp. 391–403, 1998.

107. Duhm, S., Xin, Q., Hosoumi, S., Fukagawa, H., Sato, K., Ueno, N., Kera, S., “Charge Reorganization Energy and Small Polaron Binding Energy of Rubrene Thin Films by

Ultraviolet Photoelectron Spectroscopy” *Advanced Materials*, Vol. 24, No. 7, pp. 901–905, 2012.

108. Kera, S., Hosoumi, S., Sato, K., Fukagawa, H., Nagamatsu, S., Sakamoto, Y., Suzuki, T., Huang, H., Chen, W., Wee, A. T. S., Coropceanu, V., Ueno, N., “Experimental Reorganization Energies of Pentacene and Perfluoropentacene: Effects of Perfluorination” *The Journal of Physical Chemistry C*, Vol. 117, No. 43, pp. 22428–22437, 2013.

109. Pope M., Swenberg, C. E., "*Electronic processes in organic crystals and polymers"* Oxford University Press, 1999.